# A comprehensive land surface vegetation model for multi-stream data assimilation, D&B v1.0

Wolfgang Knorr[1], Matthew Williams[2], Tea Thum[3], Thomas Kaminski[1], Michael Voßbeck[1], Marko Scholze[4], Tristan Quaife[5], T. Luke Smallman[2], Susan C. Steele-Dunne[6], Mariette Vreugdenhil[7], Tim Green[2], Sönke Zähle[8], Mika Aurela[3], Alexandre Bouvet[9], Emanuel Bueechi[7], Wouter Dorigo[7], Tarek S. El-Madany[8], Mirco Migliavacca[8,9], Marika Honkanen[3], Yann H. Kerr[10], Anna Kontu[3], Juha Lemmetyinen[3], Hannakaisa Lindqvist[3], Arnaud Mialon[10], Tuuli Miinalainen[3], Gaetan Pique[10], Amanda Ojasalo[3], Shaun Quegan[11], Peter. J. Rayner[1], Pablo Reyez-Muñoz[12], Nemesio Rodríguez-Fernández[9], Mike Schwank[13], Jochem Verrelst[12], Songyan Zhu[2], Dirk Schüttemeyer[14], and Matthias Drusch[14]

[1]The Inversion Lab, Tewessteg 4, D-20249 Hamburg, Germany
[2]University of Edinburgh, Edinburgh, UK
[3]Finnish Meteorological Institute, Helsinki, Finland
[4]Lund University, Lund, Sweden
[5]University of Reading, Reading, UK
[6]Department of Geosciences and Remote Sensing, Delft University of Technology, The Netherlands
[7]Vienna University of Technology, Wien, Austria
[8]Max-Planck Institute for Biogeochemistry, Jena, Germany
[9]DG Joint Research Centre, European Commission, Ispra, Italy
[10]Centre d'études Spatiales de la Biosphère (CESBIO), Université de Toulouse 3 Paul Sabatier, Centre National de la Recherche Scientifique, Centre National d'Etudes Spatiales, Institut de Recherche pour le Développement, Institut National de Recherches pour l'Agriculture, l'Alimentation et l'Environnement, Toulouse, France
[11]University of Sheffield, Sheffield, UK
[12]University of Valencia, Valencia, Spain
[13]Swiss Federal Institute for Forest, Snow and Landscape Research, Birmensdorf, Switzerland
[14]European Space Agency, ESTEC, Noordwijk, The Netherlands

**Correspondence:** Wolfgang Knorr (wolfgang.knorr@inversion-lab.com)

**Abstract.** Advances in Earth Observation capabilities mean that there is now a multitude of spatially resolved data sets available that can support the quantification of water and carbon pools and fluxes at the land surface. However, such quantification ideally requires efficient synergistic exploitation of those data, which in turn requires carbon and water land-surface models with the capability to simultaneously assimilate several of such data streams. The present article discusses the requirements for such

5  a model and presents one such model based on the combination of the existing DALEC land vegetation carbon cycle model with the BETHY land-surface and terrestrial vegetation scheme. The resulting D&B model, made available as a community model, is presented together with a comprehensive evaluation for two selected study sites of widely varying climate. We then demonstrate the concept of land surface modelling aided by data streams that are available from satellite remote sensing. Here we present D&B with four observation operators that translate model-derived variables into measurements available from

10  such data streams, namely: fraction of photosynthetically active radiation (FAPAR), solar-induced chlorophyll fluorescence

(SIF), vegetation optical depth (VOD) at microwave frequencies, and near-surface soil moisture, also available from microwave measurements. As a first step, we evaluate the combined model system using local observations, and finally discuss the potential of the system presented for multi-stream data assimilation in the context of Earth Observation systems.

## 1  Introduction

15  Monitoring the status of land surface carbon pools has gained significant attention following various climate related pledges to balance carbon sources and sinks (Heiskanen et al., 2022). Indeed, even though anthropogenic carbon fluxes are responsible for creating a large imbalance of the global carbon cycle that has led to sustained and accelerating greenhouse-gas forcing, the largest $CO_2$ fluxes globally are related to plant photosynthesis, plant respiration and the decay of dead plant matter (Friedling-stein et al., 2022). These carbon fluxes are determined by climatic factors, the presence and amount of photosynthesising
20  vegetation, and soil water availability, the latter due to the intrinsic water limitation of biological processes (Gerten et al., 2005).

A reliable characterisation of both carbon and water fluxes and pools at a range of spatial scales is therefore of paramount importance, as we currently lack a robust, spatially and temporally explicit knowledge of the sources and sinks of $CO_2$, or of the drivers of those variations. Current climate predictions and climate policy scenarios crucially depend on assumptions about
25  the future fate of the terrestrial carbon stores and their interaction with future climate variations, but how those variations work and interact with various forcing factors is still only partially understood (Arora et al., 2020). This makes policies that rely on future climate scenarios intrinsically unreliable.

Earth observation technology offers a powerful tool for observing the land vegetation and soil water status in multiple, complementary ways across time and space. However, there remain serious challenges for their exploitation, in particular a
30  lack of a direct link between the variable of interest and remotely sensed information. In other words, remote sensing regularly provides only an indirect measure (Disney et al., 2016; Gao et al., 2021) – with widely varying accuracy – of some underlying processes, such as photosynthetic activity, rather than a quantification of carbon pools and fluxes. Or if carbon fluxes or pools are estimated, those estimates heavily rely on models and auxiliary inputs (Running and Zhao, 2015), or have so far been validated only locally (Liu et al., 2022). Thus, we expect significant added value if those data are used within a data assimilation
35  framework, allowing the synergistic use of multiple data streams (Berger et al., 2012; Ciais et al., 2014; Scholze et al., 2017). This is particularly relevant given that remote sensing offers unparalleled data coverage over large regional to global scales at high temporal frequency.

In this study we present a process-based modelling system that is suitable for the assimilation of a wide range of such data streams, enabling a synergistic multi-data stream land surface carbon monitoring and prediction system. So far, there have
40  been a number of relevant studies, mostly using single data streams. For example, the Biosphere Energy-Transfer HYdrology scheme (BETHY, Knorr, 2000) has a long record of data assimilation studies using land surface temperature (Knorr and Lakshmi, 2001), atmospheric $CO_2$ (Rayner et al., 2005), fraction of photosynthetically active radiation (FAPAR, Knorr et al., 2010; Kaminski et al., 2012), eddy-flux measurements (Knorr and Kattge, 2005), solar-induced fluorescence (SIF, Norton et al.,

2017, 2018, 2019), the combination of $CO_2$ and passive-microwave-derived soil moisture (Scholze et al., 2016) as well as the

45 combination of $CO_2$, L-band passive-microwave soil moisture and vegetation optical depth (Scholze et al., 2019). BETHY is a combined carbon and water land surface model that focuses on faster processes, such as energy and water exchanges, and carbon fluxes at time scales from hours up to several years, coinciding with the typical time span of satellite missions. BETHY also the core of the first Carbon Cycle Data Assimilation System (CCDAS, Rayner et al., 2005; Kaminski et al., 2013). BETHY has been developed specifically for the purpose of assimilating both satellite and locally measured carbon and

50 energy flux data. The main limitation of the above studies, however, is that BETHY does not account for plant growth and allocation, and therefore cannot capture slow increases in living-plant biomass over time.

Following up from the experiences gained from the studies previously cited, we identify the following essential requirements for a process-model at the centre of the envisaged land surface carbon monitoring system:

– representation of internal processes affecting carbon, water and energy fluxes at time scales of hours to several years, to
55 permit spatial and temporal scaling;

– representation of specific variables that directly link to remotely sensed information and, if needed, related 'observation operators', i.e. modules that simulate the same variable as provided by the assimilated data stream;

– computational efficiency, high degree of simplicity while retaining sufficient realism, and ideally the availability of the adjoint model code to enable the use of efficient variational assimilation approaches.

60 We address these requirements by the development of a new process model, which combines the BETHY and DALEC (Data Assimilation Linked Ecosystem Carbon) models, both of which have been specifically designed with data assimilation in mind and have a corresponding track record. BETHY provides a detailed representation of fast and intermediate-time scale processes while DALEC provides a focus on slower processes of carbon allocation and turnover. This combination opens up the possibility of retrieving variables such as biomass carbon stocks, that were not the focus of the assimilation studies using

65 BETHY. DALEC is a mass-balance model that simulates the dynamics of live and dead carbon pools and associated fluxes (Williams et al., 2005; Bloom and Williams, 2015). DALEC has been developed specifically for assimilating information on C fluxes and pools from satellite observations (Bloom and Williams, 2015), eddy covariance systems (Bloom and Williams, 2015; Famiglietti et al., 2021), and biometric data including biomass (Smallman et al., 2017; Quegan et al., 2019). Data assimilation is used to assign parameter values and their uncertainty ranges, as well as model initial conditions, at the pixel-scale across the

70 modelled domain. DALEC requires input in the form of either gross or net primary productivity (NPP) from a separate model, in this case BETHY. In return, DALEC provides information on leaf area back to BETHY.

In this contribution we present the newly developed D&B (DALEC & BETHY) model together with original measurements from two study sites of widely varying climate and vegetation, both within the ESA-funded Land surface Carbon Cycle (LCC) study. Due to the considerable computational demands of data assimilation, D&B avoids any complexity that cannot be justified

75 by the need to improve the realistic simulation of target variables. Coupling of the two models together with their respective components, state and driving variables is shown in Section 2 (Figure 1). D&B has been developed with the specific purpose

of providing a modular and flexible modelling scheme for the assimilation of multiple data streams. We present the various components of the core model, and a detailed evaluation of the *a priori*, uncalibrated model. We also present observation operators for FAPAR, SIF, vegetation optical depth (VOD) and near-surface soil moisture, and a further evaluation of the

80    model combined with each observation operator against locally measured data, as a precursor to the use of satellite-derived Earth observation data.

## 2  Model description

The D&B model is comprised of three interconnected components: (i) photosynthesis and autotrophic respiration, (ii) energy and water balance, and (iii) carbon allocation and cycling, including heterotrophic respiration (Figure 1). The first comprises

85    processes that lead to the uptake of $CO_2$ via plant photosynthetic activity (gross primary production, GPP), influenced by temperature, light absorption across the canopy, and stomatal control, as well as carbon loss from the respiration of live vegetation ($R_A$, autotrophic respiration). The remaining carbon flux is then passed as net primary production (NPP = GPP - $R_A$) into the Carbon Allocation and Cycling component. The Energy and Water Balance determines the energy input to and output from the canopy in the form of radiative heat, latent and sensible heat transport, taking into account the water balance

90    of the canopy and soil, as well as the rate of water uptake from the roots. Components (i) and (ii) are based on BETHY, and component (iii) on DALEC.

Depending on the domain for which the model is set up, D&B distinguishes up to 13 Plant Functional Types (PFTs) as shown in Table 1. Each PFT is characterised by a unique set of parameter values. All PFTs use the C3 photosynthetic pathway, except for PFT 10, for which a separate module for C4 photosynthesis is used (see the Supplementary Information, SI, Section

95    1.1.1). Management of arable crops is represented by appropriate parameters for leaf onset and fall, as well as assumptions about a minimum level to which soil moisture is allowed to fall, as an approximation of irrigation (SI Section 1.2.7).

The fundamental model time step is 1 hour. The following components are, however, simulated at a daily time step in order to decrease the computational effort:

   – soil water balance

100   – canopy water balance

   – snow module

   – the observation operators for VOD and surface soil moisture

The model simulates several PFTs in sub-grid tiles. Each PFT is simulated separately as if it would cover the full grid cell, with the results re-scaled by multiplying them with the grid-cell fraction occupied by the specific tile. Inter-PFT competition

105   for light or water are neglected. A given grid cell can thus comprise several PFTs each with its specific cover fraction.

**Table 1.** Parameter combinations are available for the following plant functional types in D&B:

| PFT# | Short name | Description |
|---|---|---|
| 1 | TrEV | Tropical broadleaf evergreen tree |
| 2 | TrDD | Tropical broadleaf deciduous tree |
| 3 | TmEv | Temperate broadleaf evergreen tree |
| 4 | TmSg | Temperate broadleaf deciduous tree |
| 5 | EvCn | Evergreen coniferous tree |
| 6 | SgCn | Deciduous coniferous tree |
| 7 | EShr | Evergreen shrub |
| 8 | DShr | Deciduous shrub |
| 9 | C3Gr | C3 grass |
| 10 | C4Gr | C4 grass |
| 11 | TunV | Tundra |
| 12 | WetV | Wetland |
| 13 | ArbC | Arable crop |

## 2.1 Photosynthesis and Autotrophic Respiration

The C3 photosynthesis module (SI Section 1.1.1) is based on the biochemical model of photosynthesis by Farquhar et al. (1980). It determines light absorption, light-limited electron transport, $CO_2$-limited carboxylation rate and the resulting gas exchange of $CO_2$. Light absorption in the photosynthetically active spectrum is calculated within a two-flux approximation (SI Section 1.1.1), following Sellers (1985). D&B divides the canopy into several vertical layers of equal LAI, the sum of which constitutes the total canopy LAI. In the standard configuration, the number of layers is three. The amount of light absorbed and thus available for photosynthesis is dependent on LAI, statistical leaf orientation (assumed to be isotropic) and leaf single-scattering albedo. Photosynthetic capacity decreases from top to bottom of the canopy, assuming that decreasing levels of daily-average solar radiation drives decreases in leaf nitrogen content and maximum rates of light-limited photosynthesis.

The photosynthesis module further divides GPP into NPP and $R_A$ (SI Section 1.1.2). $R_A$ is modelled as the sum of maintenance and growth respiration (Knorr, 1997). While maintenance respiration is proportional to photosynthetic capacity, growth respiration is proportional to NPP, and zero when NPP is negative. Both continually increase with temperature. Negative NPP is also passed on to the C Allocation and Cycling component, where it leads to the depletion of the labile C pool.

The rate of photosynthesis is first computed under standard conditions without limitation by water availability. This potential photosynthesis rate is translated into an equivalent stomatal conductance, i.e. the stomatal conductance necessary to provide the flow of $CO_2$ to the leaf interior. This value for stomatal conductance without water limitation is reduced depending on the vapour pressure deficit of the surrounding air, and available soil moisture. This modified stomatal conductance, or "actual stomatal conductance", then determines actual photosynthesis and, using information from the Energy and Water Balance component, the rate of transpiration.

## 2.2 Energy and Water Balance

125

The Energy and Water Balance component requires the rate of transpiration from the photosynthesis module, due to the tight coupling between water loss through transpiration and $CO_2$ uptake by leaves. Transpiration (SI Section 1.2.4) is subsequently combined with other evaporative fluxes, namely of intercepted water (canopy evaporation, Figure 2, SI Section 1.2.3), and from the soil surface (soil evaporation, SI Section 1.2.5), including snow sublimation (SI Section 1.2.7), to arrive at total

130 evapotranspiration and latent heat flux. Latent heat flux is constrained by the available net radiative energy input, which the model computes separately for the vegetation canopy and the soil (SI Section 1.2.6). Sensible heat flux is computed from the assumption of energy closure from net radiation, latent and soil heat flux. The model uses incoming shortwave (solar) and longwave (thermal) radiation as input, but simulates both outgoing radiation components internally, using information on the albedo of the soil background and vegetation (SI Section 1.2.8).

135 Soil evaporation proceeds at the equilibrium rate driven by the soil net radiation from a thin surface layer. This corresponds to a typical depth for which microwave remote sensing can provide soil moisture estimates (Babaeian et al., 2019). Evapotranspiration from the canopy happens as either canopy evaporation from leaf surfaces at the equilibrium rate ($E_i$, Jarvis and McNaughton, 1986), or as transpiration through leaf pores ($E_t$). Precipitation enters either the leaf interception pool ($W_i$), or the soil pool ($W_r$ and $W_s$, see SI Section 1.2.1). Precipitation happens as either snow ($P_{sn}$, SI Section 1.2.7), or rainfall ($P_r$),

140 partitioned into a canopy-interception part ($E_i$), soil infiltration ($P_s$), and surface runoff ($Q_s$). Soil water drains as sub-surface runoff ($Q_d$), or base flow ($Q_b$). Infiltration into the soil (SI Section 1.2.2), runoff, drainage and baseflow (SI Section 1.2.5) are simulated following a new implementation of the variable infiltration capacity approach (Wood et al., 1992), where a thin surface layer has been added to a single root-zone layer, (Scholze et al., 2016). The surface soil moisture layer overlaps with the root zone layer, so that the near-surface soil water pool ($W_s$) forms part of the root-zone soil water pool ($W_r$, Figure 2).

145 The former has a nominal depth of 4 cm, the latter a depth equal to a PFT-specific root depth, $d_r$ (SI Table 1 in Section 1.1.2). Both depths are limited by depth to bedrock. Soil water exiting the root zone downwards is considered subsurface drainage, while there is no upward water movement from below the root zone. The root zone soil moisture pool contains all simulated soil water, while the surface layer is added in order to be able to calculate soil evaporation, as well as for diagnostic purposes, taking account of the impact of surface soil moisture on microwave remote sensing.

150 Once per day around the time of maximum evaporative demand, assumed to be at the hourly time step closest to 13:00 hours local solar time (Knorr, 1997), the parameters determining actual stomatal conductance are reset to reflect soil water status. To do this, transpiration is simulated as the minimum of a root water supply rate, which increases linearly as soon as soil water exceeds the permanent wilting point, and the demand for transpiration. This rate of demand is determined by the potential rate of photosynthesis without water stress. Potential photosynthesis is assumed as the rate at a fixed ratio of leaf to atmospheric

155 $CO_2$ content (0.87 for C3 and 0.67 for C4 photosynthesis). Actual photosynthesis and stomatal conductance are then set such that transpiration is capped at the root supply rate. A supply-demand calculation then determines the rate at which leaf stomata close in response to the water vapour deficit of the surrounding air.

Finally, the surface reflectance, or background albedo ($\rho_S$), is affected by soil brightness, surface soil water content, and the presence of snow. Vegetation albedo as a function of absorption in the photosynthetically active spectrum, computed in the photosynthesis module, and snow albedo is modelled depending on snow age (Loth and Graf, 1996; Knorr, 1997).

## 2.3 Carbon Allocation and Cycling

The carbon cycle in D&B is expressed as a series of six equations describing the dynamics of six carbon pools. Other than the original DALEC model, D&B employs an hourly time step for allocation, the same as the time step used by the photosynthesis module. There are four live C pools, for foliage (*fol*), wood (*wd*) and fine roots (*fr*), a labile (*lab*) pool which supports foliage expansion, and two dead organic matter pools, namely litter (*lit*) and soil organic matter (*SOM*). The state equations describe the change over time in pool sizes on the basis of C fluxes in and out of the pool. Carbon inputs all derive originally from NPP. NPP is allocated to each of the four live biomass pools based on fixed site of PFT-specific fractions.

The labile C pool in D&B represents the stored C used to initiate accelerated leaf development at the start of the growing season (SI Section 1.3.1). The phenology scheme parameterises timing of local bud burst via allocation to leaves from the labile pool based on calibrated climate sensitivity. Leaf development thus depends on the allocation of labile carbon, replenished from NPP, to the leaf carbon pool in addition to direct allocation from NPP. The leaf area index is determined by the conversion of leaf carbon pool size to leaf area by way of fixed values of leaf mass per area.

The fine root (*fr*) and wood pools (*wd*) are determined by first-order differential equations, using a decay constant combined with an fractional input, again from NPP (SI Section 1.3.2). Thus, a fraction of the fine root pool replenishes the litter pool, added by strongly periodic inputs linked to leaf senescence, while wood directly feeds SOM. The litter pool decays either to $CO_2$ via heterotrophic respiration, or is transferred to the SOM pool. Mineralisation of both SOM and litter C pools by heterotrophic respiration thus results in further $CO_2$ fluxes. Total ecosystem respiration (TER) is determined by the sum of autotrophic growth and maintenance respiration, and mineralisation of dead organic matter (*lit* or *som*), creating a flux of heterotrophic respiration. Following the procedure used for DALEC, the prior parameters of the Carbon Allocation and Cycling are set through a regional-scale calibration procedure, as described in SI Section 1.3.3.

## 3 Observation Operators

The task of an observation operator is to simulate the equivalent of an observation from the model's state variables. This includes the simulation of the variable that is retrieved at the time when it was observed and over the footprint of the observations (Kaminski and Mathieu, 2017). In this manuscript, we will present the simulation of four data streams, namely FAPAR, SIF, L-band VOD and near-surface soil moisture, and then confront model simulations with local measurements. Of the four data streams, FAPAR and surface soil moisture are internally calculated.

## 3.1 Fraction of absorbed photosynthetically active radiation (FAPAR)

FAPAR is a measure of the capacity of terrestrial vegetation to absorb sunlight in the visible spectrum, i.e. that part that can be utilised as photosynthesis. It is defined as the amount of photosynthetically active radiation (PAR) absorbed by green, functioning leaves divided by the total incoming PAR. FAPAR is calculated within the two-flux canopy radiative transfer scheme (SI Section 1.1.1) required for the calculation of GPP (Section 2.1). However, due to the dependence of FAPAR on solar zenith angle, it is necessary to take into account the solar zenith angle at time of observation. Therefore, the observation operator for FAPAR needs to insure that either a separate calculation of FAPAR at the correct solar zenith angle is performed, or it utilizes FAPAR calculations from the model run at the times and dates where model and observations solar zenith angles match.

## 3.2 Solar Induced Fluorescence (SIF)

Strictly speaking, the canopy level solar-induced chlorophyll fluorescence, or SIF, is a measure not of the photosynthetic rate as such, but of the amount of radiation absorbed by the leaf and not used for the purpose of photosynthesis. Some of that surplus radiation is re-emitted as fluorescent light as part of a copying mechanism of the photosynthetic system. Under normal field conditions, however, SIF can often be used as an indication of photosynthetic activity, as opposed to FAPAR, which only characterises the photosynthetically active light that is potentially available (Porcar-Castell et al., 2014; Mohammed et al., 2019).

To calculate SIF, we use the formulation of Gu et al. (2019). This choice is motivated by the direct link to the photosynthesis routines and the relatively parsimonious implementation, which fits with the modelling strategy adopted here. The canopy layer SIF, $S_n$, is given by:

$$S_n = s_{SIF} J_n \frac{1 - \psi_{PSIImax}}{q_L \psi_{PSIImax}(1 + k_{DF})}, \tag{1}$$

where $J_n$ is the electron transport in canopy layer $n$ (SI Equ. 8), $\psi_{PSIImax}$ is the maximum photochemical quantum yield of photosystem II, $q_L$ is the fraction of open photosystem II reaction centres and $k_{DF}$ the ratio of the first order rate constants for heat dissipation and fluorescence. We take the values prescribed by Gu et al. (2019). Note that the original equation in that paper also has a term for the photon escape probability from the canopy. In D&B, this is calculated explicitly by the layered 2-stream model (SI Section 2) and hence is not required here. As an extension to the model by Gu et al. (2019) in view of the anticipated calibration in a data assimilation scheme, we further introduce the scaling factor $s_{SIF}$, which compensates for large uncertainties in (1) the values of the three constants $\psi_{PSIImax}$, $q_L$, and $k_{DF}$ and (2) the spectral conversion that is described below. We set the prior value of $s_{SIF}$ to 1.

SIF produced by the D&B model via the layered 2-stream model described in Section 2 of the SI has native units of $mol.m^{-2}s^{-1}$. It represents the total flux of photons into the hemisphere above the canopy for all wavelengths. Satellite measurements and *in situ* observations, however, are typically recorded in energy flux units per steradian, per nano-metre of the SIF

spectra, e.g. $Wm^{-2}s^{-1}nm^{-1}sr^{-1}$. To convert from molar to energy units, we apply the molar form of the Planck equation, providing energy per mole of photons, $e$. ($e = ahc/\lambda_\phi$, where $a$ is Avogadro's number, $6.023 \times 10^{23}$, $h$ is the Planck constant, $6.626 \times 10^{-34}\ m^2kg.s^{-1}$), $c$ is the speed of light, $3.0 \times 10^8\ m.s^{-1}$ and $\lambda_\phi$ is the wavelength of the SIF photons in metres.

We convert to steradians by using a constant factor of $\frac{1}{2\pi}$, which assumes that the emittance of SIF from the top of the canopy is isotropic, and finally weight by the relative strength of emissions at $\lambda_\phi$ compared to a reference SIF spectrum, i.e.:

$$w = \frac{E(\lambda_\phi)}{\sum_i E(\lambda_{\phi,i})}, \tag{2}$$

where $E$ is the SIF emission spectrum of arbitrary units. Hence:

$$SIF' = SIF\frac{ew}{2\pi}, \tag{3}$$

Where SIF has units of $mol.m^{-2}s^{-1}$ and $SIF'$ has units of $Wm^{-2}s^{-1}sr^{-1}nm^{-1}$.

For the present study we use a SIF emission spectrum observed at the Hyytiälä site in Finland (Magney et al., 2019). The SIF spectrum was measured for four Scots pine trees at light level of 1200 $\mu mol m^{-2}s^{-1}$ and then averaged.

### 3.3 Vegetation optical depth (VOD)

Vegetation optical depth (VOD) is essentially a parameter describing the attenuation of microwave radiation at some wavelength due to the presence of vegetation. It depends on the dielectric properties (due to water content, temperature and chemical composition) as well as the structure and geometry of the vegetation, and sensor properties (e.g. wavelength, polarization). Due to the relatively static nature of structure, dynamics of VOD are generally attributed to changes in above ground biomass and water content (Ulaby and Wilson, 1985; Konings et al., 2019). It is measured within the microwave spectrum with passive instruments, using the black body radiation of the surface in the microwave domain), or active instruments such as scatterometers or synthetic aperture radars.

Common retrieval methods may extract both the surface soil moisture and VOD simultaneously from satellite remote sensing data, provided enough measurements are performed. For example the SMOS (Kerr et al., 2010) retrieval algorithm (Kerr et al., 2012) is based on the so-called $\tau - \omega$ formulation for the vegetation contribution (Kirdiashev et al., 1979; Mo et al., 1982) of the microwave signal, where VOD is denoted by $\tau$, the perpendicular vegetation optical depth (Wigneron et al., 2007, 2010).

Here, however, we compare simulations to locally measured L-band passive VOD measurements. Due to the local setup where separate sensors are placed above and below the canopy (see SI Section 3.6), it is possible to measure VOD directly without having to solve for soil moisture simultaneously. We use a semi-empirical formulation for L-band VOD, expressed as:

$$\tau_\lambda = f(T)(l_{wd}C_{wd} + l_{fol}C_{fol})(l_s f_{soil} + l_f f_E + l_0), \tag{4}$$

**Table 2.** Parameters for empirical observation operator for L-VOD.

| Parameter | Unit | Value |
|---|---|---|
| $l_{wd}$ | m$^2$/gC | $2.0 \times 10^{-4}$ |
| $l_{fol}$ | m$^2$/gC | $2.0 \times 10^{-4}$ |
| $l_s$ | - | 1.20 |
| $l_f$ | - | 4.0 |
| $l_0$ | - | 0.4 |

where the subscript $\lambda$ denotes its wavelength dependence, $C_{fol}$ and $C_{wd}$ are the leaf and woody biomass pools, respectively (see SI Section 1.3.2), $f_{soil}$ (SI Equ. 91) is fractional plant-available soil water content, and

$$f_E = E_t/E_{t,max} \tag{5}$$

i.e. the ratio of actual to potential transpiration (see SI Equs. 59 and 64). $f_{soil}$ describes slow changes in the plant's hydrological
250   status, hence multiplied by parameter $l_s$, and $f_E$ fast changes, multiplied by parameter $l_f$. The other empirical parameters are $l_0$, $l_{wd}$ for dependence on woody biomass, and $l_{fol}$ for dependence on leaf biomass.

Following Schwank et al. (2021), we include an explicit temperature dependency in the form of:

$$f(T) = 0.25 + 0.75/(1 + e^{-0.5(T+3)}), \tag{6}$$

which approximates theoretically derived behaviour around the freezing point, with $T$ being 2-m air temperature. This for-
255   mulation can be used across a range of microwave wavelengths, using different parameter values in each case. The second multiplicative factor in Equ. (4) is an empirical, linear expression using both woody and foliar biomass with the assumption that VOD will be zero if no biomass is present. The third multiplicative factor describes how the water status of the vegetation modifies this expression. This last one also contains a constant factor, $l_0 > 0$, because we expect positive VOD even if vegetation water stress is at its maximum.

260   In this contribution, we apply it to passive L-band microwave measurements. The parameters for the empirical VOD observation operator, shown in Table 2, were chosen to reproduce a reasonable fit to L-band observations from SMOS over bptj the Sodankylä and the Majadas del Tietar sites.

### 3.4 Near-surface soil moisture

In the D&B model, near-surface soil moisture is represented by an explicitly modelled thin surface soil moisture layer, with
265   a depth of 4 cm, unless depth-to-bedrock indicates a lower value. It is therefore a state variable in the model's soil water component, and is described in detail in Section 2.2. This surface layers therefore here serves a dual purpose, to diagnose a variable that can potentially be used as an assimilated data stream, and to simulate soil evaporation.

Near-surface soil moisture data is usually available from passive data when retrieved simultaneously with VOD. These retrieval algorithms explicitly separate the contributions to the microwave signal that come either from the vegetation (VOD)

270   or from the soil (surface soil moisture).

## 4   Model evaluation

We first present an evaluation of the D&B model on its own, followed by an evaluation of the model together with the observation operators for the four data streams FAPAR, SIF, L-VOD and surface soil moisture. The methods used to derive the driving data for the model as well as those of the measurements undertaken for model evaluation are described in Section 3 of the SI.

275   ### 4.1   Study sites

The D&B model is run for two study sites, one representing a boreal forest – Sodankylä in Finland, a Class 1 site of the ICOS network (Rebmann et al., 2018) – the other representing a temperate savanna ecosystem – Majadas de Tietar in Spain, also an ICOS network site. The Sodankylä Scots pine forest site ($67^o21'44.6"$N, $26^o38'18.9"$E) is situated 100 km north of the Arctic Circle (Thum et al., 2007; Honkanen et al., 2023). It also has an understory of evergreen ericacecous shrub (mostly blueberry)

280   as well as lichen and mosses. The soil is characterised as predominantly sand (0-10 cm: 0.5/6.0/88.1/5.4% clay/silt/sand and stone, respectively; 10-20 cm: 0.3/4.1/93.5/2.1%; 20-40 cm: 0.2/2.8/91.9/5.1%.

The Majadas de Tietar site is a Mediterranean open woodland of evergreen Holm oak in western Spain ($39^o56'24.68"$N, $5^o45'50.27"$E,  Wang et al., 2016; El-Madany et al., 2018). The soil (Nair et al., 2020) contains an upper sandy layer (5% Clay, 20% silt, 75% sand, 20 cm deep) underlain by a clay layer (30 to 60 cm depth, no information for 20 to 30 cm).

285   ### 4.2   Model setup

The model simulation was run for the period 1 Jan 2009 to 31 Dec 2021 for Sodankylä, and 1 Apr 2014 to 31 Dec 2021 for Majadas de Tietar with *a priori* values of the parameters for all modules and observation operators. Initial water content of the soil was set to 50% of field capacity. Simulations for the first two calendar years (2009 and 2010 for Sodankylä, 2014 und 2015 for Majadas de Tietar) were discarded to avoid model biases due to initial conditions of the water balance and short-lived

290   carbon pools.

For Sodankylä, the model is run with two PFTs, evergreen coniferous forest (PFT 5, 67% of ground area) and evergreen shrub (PFT 7, 33%). For Majadas del Tietar, we assume the site area to comprise C3 grass (PFT 9, 80% of ground area) and temperate evergreen trees (PFT 3, 20%). The fractional vegetation cover is set to $f_c = 1$ for both sites.

We use locally observed data to drive the model (see SI Section 3.1). $C_a$ is set to a uniform value of 405 ppm, i.e $C_a = $

295   $405 \times 10^{-6}$mol($CO_2$)/mol(air), which is approximately the annual mean value at Mauna Loa, Hawaii, centered around the beginning of 2017 (NOAA, 2024). Measured soil temperature as model input at Sodankylä is for 1 m depth. At Majadas del Tietar, the model is driven by soil temperature measured at 80 cm depth averaged between four two locations, two in open grassland and two under a tree canopy.

The soil texture class is "medium/coarse" for Sodankylä and "medium" for Majadas del Tietar (cf. SI Section 1.2.5, Table 4), following the classification of the global soil texture data set by Zobler (1986).

### 4.3 Evaluation approach

The D&B model is compared against eddy covariance data of carbon and energy fluxes, locally observed radiation balance, and, in the case of the boreal site, snow depth. This is a first evaluation of the model with its *a priori* parameterisation and its purpose is to assess whether the model is able to reproduce measurements with a reasonable degree of realism. The role of the in situ observations is to serve as an independent evaluation data set. We compare multi-year averages of the annual cycle, multi-year mean, and also use as a measure of comparison the explained variance ($r^2$) and root-mean square error (RMSE) at the daily and annual time scales, where model and measured values are statistically compared on the basis of daily or annual averages, respectively. An outlook at setting up D&B together with its observation operators within a data assimilation framework is giving in Section 6.

Carbon fluxes are gross primary productivity (GPP), total ecosystem respiration (TER), and net ecosystem exchange (NEE=TER-GPP). NEE is defined as going from the vegetation to the atmosphere, i.e. positive values denote a flux of $CO_2$ towards the atmosphere. Energy fluxes are latent heat flux (LHF) and sensible heat flux (SHF), with the addition of net radiation, which is the balance of incoming minus outgoing solar and thermal radiation fluxes. Both carbon and energy fluxes, and net radiation are measured over a representative area of each ecosystem, consisting of different PFTs.

The length of comparison is 6 years (2016 to 2021) for both sites. We additionally use snow depth measurements from the period 2011 to 2021 for validation at the Sodankylä site. Biomass and soil carbon measurements, also at the Sodankylä site, were taken in 2011, and are compared to mean values of the simulations form 2011 to 2021 (Sodankylä) or 2016 to 2021 (Majadas del Tietar). See SI Section 3 for details of measurement methods.

### 4.4 Evaluation at Boreal forest site: Sodankylä

At the boreal-forest site (Figure 3), measurements show a markedly smaller amplitude of the annual cycle of carbon fluxes (NEE) than to the model. While in the spring time, there is a reasonable agreement with an initial rapid increase in the magnitude of NEE, carbon loss during the winter, and carbon uptake during summer and early autumn are clearly larger for the model. Between DOY 200 and 260 (mid July to mid September), the discrepancy in NEE is associated with an underestimate by the model of respiration (TER) and an overestimate of GPP. Not surprisingly, GPP agrees well during the winter as it is well constrained due to the lack of light and low temperatures, but TER is generally higher for the model. There is also a conspicuous phase shift of TER between the two curves, with measurements showing TER peaking much later, while the phases of GPP agree reasonably.

For the energy flux evaluation (Figure 4), what stands out is the good agreement between modelled and simulated net energy input (i.e. net radiation minus ground heat flux, cf. SI Equ. 124. 127). LHF is also well matched, except during the early spring (ca. DOY 50 to 100), where the model underestimates the early onset of evaporative fluxes. SHF is well matched during the summer, but overestimated during winter and spring. Correspondingly, there is slight overestimate of the net radiation during

winter. The fact that net radiation is also overestimated during the summer while both LHF and SHF math very well also deserves attention: the energy balance is by definition exactly matched by the model (i.e. SHF plus LHF equal net radiation minus soil heat flux). Therefore, we attribute the mismatch in net radiation during the summer to a lack of energy closure of

335   the eddy covariance measurements.

Another noteworthy period is the winter time, where the model produces slightly negative SHF and at the same time overestimates LHF compared to observations. Both deviations about cancel each other, and there does not seem to be an issue with energy closure for the observations.

Snow depth observations taken from within the forest and simulated snow depth for the evergreen conifer tree PFT agree

340   generally very well with each other (Figure 5). The model tends to somewhat underestimate the observations, especially at the time of snow melt, where snow depth is receding, but the differences are small and the comparison favourable, in particular when noting the good agreement in interannual variations. The peak winters with highest values (e.g. the winter 2019/2020) are also well reproduced.

On an annual average basis, modelled NEE shows a small carbon sink with NEE equal to -197 $gCm^{-2}yr^{-1}$, against a smaller

345   source in magnitude for the measurements of +34 $gCm^{-2}yr^{-1}$ (values given in Table 3 converted from molar units). GPP is 534 $gCm^{-2}yr^{-1}$ observation-derived against 927 $gCm^{-2}yr^{-1}$ for the model. In contrast to the mean, the explained variance, $r^2$, is not sensitive to the absolute magnitude of the fluxes, and since the phases agree well (Figure 3) it is not surprising that it shows a very high value of 0.87 for GPP at the daily time step. For TER, however, due to the phase shift previously discussed, we find a lower value ($r^2 = 0.69$). The value of $r^2$ for NEE is smaller than for GPP and TER, as we would expect, because

350   NEE is the difference of two larger fluxes and has therefore a much smaller magnitude. (If we assume for example that the true NEE is zero, while each, the model and the measurements, reproduce broadly GPP=TER, but add some "noise" or model error to it, both of which are uncorrelated, then we would expect the model-measurement correlation for NEE to be zero, but substantial, depending on the level of the noise added, for GPP or TER.)

The value of the annual $r^2$ in Table 3 captures exclusively interannual variations and the values are much smaller than

355   derived on the basis of daily averages. It appears that the model only partially reproduces the observation-derived interannual variability, especially for NEE. Note, however, that the number of data points is only 6. RMSE for GPP and NEE on a daily basis is similar to the annual mean GPP, likely due to day-to-day variations in the measurements not being captured by the model.

Over all seasons, the model shows much higher LHF than the measurements, but much lower SHF (Table 3). The difference

360   comes almost entirely from the winter and spring seasons, as noted when discussion Figure 4. $r^2$ are also significantly smaller for energy than for carbon fluxes (Table 3) due to the seasonally varying model-observation differences, which creates differing seasonal cycles between the two. By contrast, snow depth shows a very high $r^2$ at both the daily and the annual time scale, as it was apparent from Figure 5.

Modelled carbon pools differ substantially from locally derived values: The mean and standard deviation of total soil organic

365   carbon found was 3.70±0.16 kgC m$^{-2}$, against a model-based estimate of 38.7 kgC m$^{-2}$. It appears that the model underestimates turnover time of the slowest soil carbon pool. The observed above-ground biomass at the site was 37.3 t/ha and against a

**Table 3.** Metrics for the different variables simulated at Sodankylä for the period 1/2016 to 12/2021. RMSE: root-mean square. Units: $\mu$mol m$^{-2}$ s$^{-1}$ (Gross primary productivity, GPP; total ecosystem respiration, TER; net ecosystem exchange, NEE), W m$^{-2}$ (latent heat flux, LHF; sensitive heat flux, SHF), cm (snow depth).

| Metric | GPP | TER | NEE | LHF | SHF | Snow depth |
|---|---|---|---|---|---|---|
| $r^2$ daily | 0.87 | 0.69 | 0.51 | 0.39 | 0.50 | 0.78 |
| $r^2$ annual | 0.49 | 0.26 | 0.12 | 0.36 | 0.55 | 0.84 |
| RMSE daily | 1.86 | 0.89 | 1.55 | 26.97 | 41.57 | 14.57 |
| RMSE annual | 1.09 | 0.52 | 0.63 | 16.00 | 9.63 | 6.88 |
| observed mean | 1.38 | 1.46 | 0.09 | 22.74 | 28.87 | 21.82 |
| model mean | 2.45 | 1.92 | -0.52 | 34.64 | 19.23 | 15.22 |

model estimate of 62.5 t/ha, assuming 50% carbon content of dry mass and 85% of woody biomass above ground (Helmisaari et al., 2002).

### 4.5 Evaluation at Temperate savannah site: Majadas de Tietar

370 The seasonal course of carbon exchanges at the temperate-savannah site (Figure 6) is characterised by a pronounced spring-time net carbon uptake and a prolonged period of carbon loss during the summer and autumn. However, the strength of the spring draw-down (ca. DOY 50 to 150) derived from the observations is much lower than the model-derived one. For the remaining seasons, model and observed NEE largely agree in terms of magnitude and timing, except for pronounced fluctuations in the measured NEE flux during summer and autumn that are not reproduced by the measurements, and are found in the observation-

375 derived TER flux. The discrepancy in the spring draw-down appears to be the result of a model over-estimate of GPP combined with an under-estimate of TER.

If we consider the climate of the site, with hot-dry summers, cool winters, and a winter rainfall maximum, we can assume that the most favourable growth conditions happen in the spring, where we indeed find the largest net CO$_2$ uptake rate in both model and observations. Under those spring-time conditions, however, the model predicts a higher GPP then the observation-

380 based value, but a lower GPP value for the remaining seasons where growth is either temperature and light (winter/autumn) or water (summer/autumn) limited. In other words, compared to the observations, the model over-predicts GPP under favourable conditions, but under-predicts GPP under conditions of GPP limitations — by way of dry conditions in the summer, low light levels in the autumn and temperature during winter. We thus find that the model likely overestimates moisture limitation, and also other GPP limiting factors.

385 On an annual basis (Table 4), simulated carbon fluxes are generally smaller in both directions compared to observations, with a simulated GPP and TER of 844 and 814 gC m$^{-2}$ year$^{-1}$, respectively, against eddy-covariance derived values of 1283 and 1264 gC m$^{-2}$ year$^{-1}$, respectively. Net flux (mean NEE) is small and agrees well (-30 vs. -19 gC m$^{-2}$ year$^{-1}$ for model

**Table 4.** Metrics for the different variables simulated at Majadas de Tietar for the period 1/2016 to 12/2021. RMSE: root-mean square. Units: $\mu$mol m$^{-2}$ s$^{-1}$ (Gross primary productivity, GPP; total ecosystem respiration, TER; net ecosystem exchange, NEE), W m$^{-2}$ (latent heat flux, LHF; sensitive heat flux, SHF)

| Metric | GPP | TER | NEE | LHF | SHF |
|---|---|---|---|---|---|
| $r^2$ daily | 0.61 | 0.47 | 0.27 | 0.31 | 0.81 |
| $r^2$ annual | 0.16 | 0.26 | 0.54 | 0.56 | 0.66 |
| RMSE daily | 2.11 | 1.56 | 1.88 | 30.12 | 54.37 |
| RMSE annual | 1.19 | 1.23 | 0.16 | 7.35 | 40.49 |
| observed mean | 3.39 | 3.34 | -0.05 | 39.87 | 40.10 |
| model mean | 2.25 | 2.16 | -0.09 | 32.87 | 80.49 |

vs. observations). In contrast to Sodankylä, $r^2$ for the annual values shows that the interannual variability of NEE is reproduced well, in fact better then that for the components GPP and TER. However, daily $r^2$ is much lower for NEE than for GPP or TER,
390    due to the different shape of the seasonal cycle of the model, showing a pronounced spring draw-down, as already discussed. RMSE of GPP and NEE on a daily basis is similar in magnitude to the modelled, but less than the observed mean, while annual RMSE for NEE is remarkably low, which, together with the high $r^2$, suggests that the model reproduces the interannual variability of the net carbon fluxes well for this site.

     As far as the energy balance is concerned, we find a similar result for Majadas de Tietar compared to the boreal-forest site
395    (Figure 7): net energy input (net radiation radiation minus ground heat flux) agrees very well between model and observations, but there is a rather large over-estimate by the model of the sensible heat flux, albeit with a very similar shape of the seasonal cycle ($r^2 = 0.81$, SHF daily, Table 4). For most of the year, except for a pronounced summer decline for the model but not for the observations, LHF agrees well. This is likely related to the model's pronounced under-prediction, compared to the observations, of GPP, resulting in a lower transpiration flux through more pronounced stomatal closure, and thus also lower
400    LHF. Given strict energy closure for the model, if net energy input and LHF agree between model and measurements, then SHF should also agree. However, while the model has exact energy closure, the data apparently do not. For instance, at the start of the years until ca. DOY 130, net radiation and LHF agreement suggests an imbalance starting close to zero at the start of the year increasing to around 40 Wm$^{-2}$. During the summer season, the model overestimates SHF by around 100 Wm$^{-2}$, but underestimates LHF by only around 60 Wm$^{-2}$, while net radiation agrees, which also suggests a deviation from energy
405    closure of around 40 Wm$^{-2}$. This has again to be taken into account when evaluating the model.

     On average (Table 4), the model slightly underestimates LHF, but overestimates SHF by close to a factor of two. For both LHF and SHF, we find high values for $r^2$ based on annual averages, and a very small value for annual RMSE for LHF, which suggest that the model, apart from a general overestimate of LHF, simulates interannual variability of energy fluxes reasonably well, with the caveat that only six full years are being considered here.

## 5  Evaluation of observation operators

### 5.1  Evaluation of FAPAR simulations

The simulations showed larger FAPAR values during the summer than the observations (Figure 8), with a pronounced seasonal cycle. We find this to be a robust feature of the simulations (not shown). By contrast, observed values stay at approximately the same level during the observation period, with some larger values during the autumn. The pronounced seasonal cycle of FAPAR in the model runs corresponds to a seasonal cycle in the LAI of the model. By contrast, measured FAPAR shows only weak signs of seasonality, such as a very slight increase between DOY 170 and 200. There is, however, a cluster of elevated measured FAPAR values towards late summer/ autumn, alternating with lower values in line with those measured earlier. Here we must take into account that maximum solar elevation towards the end of the measurement period (22 October) did not exceed $12^o$. Therefore, rays of direct sunshine have a longer path through the canopy, increasing FAPAR. The effect is seen to a lesser extent also in the simulations, but with an LAI driven seasonality dominating the time course of the data.

Extensive LAI sampling during the summer 2022 from hemispherical photographs give an average value of 1.37, and measurements using Li-Cor LAI-2200 an average value 1.32. These agree rather well with a simulated annual-average LAI of 1.3 for the tree PFT, however, there is a pronounced seasonality of simulated LAI corresponding to the seasonality of FAPAR seen in Figure 8, with significantly lower values for September (DOY 244 to 273: 1.37) than for mid June to the end of August (from DOY 166 to 243: 2.96). The across-plot average at different dates from the hemispheric photographs show no such seasonality, with a June to August average (measured on DOY 166, 192, 207, 212 and 217) of 1.39 vs. a September average of 1.34 (measured on DOY 254 and 271).

### 5.2  Evaluation of SIF simulations

SIF measurements provide an opportunity to document the presence of photosynthetically active plant material, and are therefore an interesting quantity for model validation. At the Sodankylä site, the observations started in spring 2021 as part of the LCC campaign activities. The measurement angle was adjusted in early June and therefore we show comparisons to the simulations starting only from June 3 onwards.

Simulated SIF values are shown here (Figures 9 to 11) with a multiplication factor of 10, i.e. with the scaling factor $s_{SIF}$ in the SIF source term, Equ. (1), set to 10. Observations are shown for two methods of retrieving SIF from the actual measurements, namely Frauenhofer line discrimination and spectral fitting (see SI Section 3.5).

At the Sodankylä site, the simulations are able to track both the diurnal and seasonal cycles of the observations reasonably well (Figure 9). However, there are indications of water stress in the measured diurnal cycles in June, July and August. These are shown in as a dip in far-red SIF during midday (Figure 9a), and for June also in red SIF (Figure 9b). The decline in SIF is likely due to midday depression of photosynthesis (Lin et al., 2024). The model reproduces this behaviour only for June and to a much lesser extent. Also, the model shows larger SIF signals for June compared to July, but not the measurements. Since mid-day depression is observed as a response to stomatal closure due to water stress, the comparison indicates that the model

underestimates water stress at the boreal site. The simulations also show an earlier increase and later decrease during the day during the summer months. This may partly be attributed to retrieval problems for high sun zenith angles.

The measured far-red SIF (760 nm) of the trees at Majadas de Tietar site (PFT 3, Figure 10a) shows a clear seasonal cycle of
445 SIF peaking in July. For red SIF (687 nm, Figure 10b), there is no clear seasonal maximum. This is independent of the retrieval method. The model by contrast shows a clear peak in May. The diurnal cycle of SIF in the model peaks later, usually around 2 pm, and extends further into the afternoon compared to the measurements, which peak around 11am to 12pm (central vertical line).

By contrast, the SIF measurements on grass (PFT 9) show almost complete senescence of the grass during June and July
450 when using the spectral fitting method, but some remaining activity when using Frauenhofer line discrimination of the red-spectrum signal (Figure 11). For this combination, red SIF with Frauenhofer line discrimination, model simulations are in good agreement with the measurements, with suitable scaling factor $s_{SIF}$ in the SIF source term (Equ. (1)). However, judging from the other spectral bands or retrieval methods, the results suggest that the model may under-estimate the water stress of the grasses.

455 ## 5.3 Evaluation of VOD simulations

Figure 12 shows the comparison between observed and simulated L-VOD for the period after the first change in measurement geometry, for all three elevation angles. Observations only include the trees, and therefore simulated L-band VOD is for the tree PFT only. The temporal variations of the measurements are well captured by the simulation, in particular after the second change in viewing geometry after DOY 280.

460 The increase in biomass in the field of view through the first change in measurement geometry on 17 September (DOY 260) was estimated to be a factor of three (see SI Section 3.6). The revised field of view was also found to better represent typical conditions of the wider area, with the initial field of view capturing the signal from much sparser vegetation. To simulate L-VOD for the period before DOY 260, we therefore reduce assumed biomass entering the VOD observation operator ($C_{wd}$, $C_{fol}$ in Equ. (4)) to one third of their default modelled values.

465 With this provision, the simulations match both temporal variations and magnitude of the locally measured L-VOD rather well (Figure 13, see SI Section 3.6 for the default simulations). This includes the rise in spring, including a peak around DOY 60, and also temporal variations between DOY 90 and 130. Only ca. DOY 130 to 180 shows a systematic overestimate compared to measurements. A slow decline after DOY 220 is also reproduced by the model. We thus find a very satisfactory performance of the empirical L-VOD observation operator together with D&B.

470 ## 5.4 Evaluation of surface soil moisture

Measured soil moisture at Sodankylä (Figure 14) shows very similar temporal variations between different depths. The temporal variations of the D&B simulations are also similar, only that the overall magnitude differs, even though the magnitude of the shallowest measured depth (5 cm) is closest to the model. We point out that the depth of the surface layer in D&B is 4 cm. Both

measurements and simulations also indicate significant interannual variability, with some years (e.g. 2019, 2020) exhibiting
some pronounced summer drying, of which only some is captured by the measurements due to data gaps.

At Majadas de Tietar, variations in soil moisture measured between different depths are again relatively small, showing
that the exact depth for which these are simulated is of lesser importance (Figure 15). In fact, the two depths closest to the
surface (5 and 10 cm depth) show an almost identical temporal profile, including the maximum soil moisture depletion during
the summer (July, August). The main characteristics of the observed seasonal cycle are also well reproduced by the D&B
model. The timing of individual rain events can be well traced in the measurements, and is well reproduced by the simulations,
including the lack of such events during the summer months. However, in the simulations, soil moisture decreases to near zero,
whereas according to the measurements some soil moisture remains even at the peak of the summer.

## 6 Discussion

### 6.1 Implications of study results

The comparison of the model simulations at the two sites against local data indicates that D&B does a reasonable job at
representing energy and carbon fluxes between the atmosphere and terrestrial vegetation. The comparison shows that carbon
fluxes in particular are simulated reasonably well, with lesser agreement for energy fluxes but also significant imbalances
between the measured energy fluxes and the net radiation available to the canopy, i.e. there is a significant deviation from
energy closure. We conclude that there is a need for multi data sources to be used for evaluating carbon and water flux models
of terrestrial ecosystems, as opposed to relying chiefly on eddy covariance data.

The addition of dedicated observation operators led to further insights regarding model performance. In particular, local SIF
measurements further revealed the power of those measurements to detect limitations on photosynthesis, such as water stress,
beyond the capability of FAPAR measurements, and this despite remaining uncertainties regarding the absolute magnitude of
the simulated SIF signal (see Figure 9). We were able to identify a possible under-estimate of soil water limitation of the Scots
Pine forest as Sodankylä during the summer, which may partly explain why the model overestimates GPP at this site.

At the Majadas de Tietar temperate savannah site, we clearly identified that the model underestimates latent heat flux during
the summer months, while it also underestimated the site's overall photosynthetic uptake (GPP). This underestimate appears to
be a result in particular of the model over-estimating moisture limitations of the savanna ecosystems during the summer, possi-
bly due to non-matching parameterisation of the stomatal model. This matched the insights provided by the SIF measurements
that the trees of the ecosystem continue transpiring and photosynthesising across the summer without major limitations due to
water stress. Surface soil moisture data also indicated too much soil drying during the summer months. Possibly, the model
fails to represent the strongly heterogeneous soil texture at Majadas del Tietar, with a sandy top and deeper clay soil, under-
estimating the soil water holding capacity of the deeper soil layers to which only the trees have access. These considerations
demonstrate the added value of the dedicated observation operators for the evaluation of D&B at the local scale.

## 6.2 Potential for further applications

The process model in combination with its observation operators presented here has been designed to be used within a variational data assimilation framework, planned to be set up following the existing CCDAS (Rayner et al., 2005). This means that D&B will be complemented with tangent and adjoint versions, which efficiently provide derivative information for variational assimilation. The anticipated default setup in data assimilation mode is for combined calibration, i.e. adjustment of parameters of the process model, its observation operators and of the initial state of the carbon pools. Assimilated data streams are planned to come chiefly from Earth Observation sources. This setup will provide both capabilities for assimilating more data streams than previous studies (e.g. Scholze et al. (2019)), while also including a full description of biomass pools as so far provided by other, more complex process models, e.g. LPJ-GUESS (Smith et al., 2001), albeit with lesser data assimilation capabilities.

In anticipation of such an application, we have in this contribution refrained from adjusting individual parameters "by hand" in order to improve the match to any of the validation data sets used in Sections 4 and 5. However, we can already assess, to an initial degree, the potential of the system to obtain a superior fit to measurements by way of optimising its parameters. As an example, comparing measured and simulated surface soil moisture (Section 5.4) and taking into account model's functional dependencies, we can infer that changing the assumed texture of the soil near its surface will immediately change the absolute magnitude of the simulated signal, but have only a negligible impact (via soil evaporation) on its temporal course.

In particular the good match between simulated and locally measured L-VOD, which includes details of most temporal variations, offers considerable opportunities for the assimilation of widely available satellite-derived L-VOD over larger regions.

## 6.3 Limitations

While the initial task to match and compare modelled and observed data streams was successfully demonstrated, the results of this study also point at the need to further investigate the seasonal cycle of LAI in northern evergreen conifer forests. In this context, it is important to note that the phenology scheme of D&B has the flexibility to simulate vegetation with a small amount of seasonal variation in LAI, if corresponding information is provided for the prior calibration of the parameters in the phenology scheme. The seasonality of LAI in D&B depends on the way DALEC is trained on remotely sensed observation. It remains to be seen to what extent those data were affected by seasonally varying observation conditions.

Another issue that occurred is that the scaling factor $s_{SIF}$ in the SIF source term (Equ. (1)) is highly uncertain. In a data assimilation mode, it would be included (possibly in PFT-specific form) into the list of parameters to be adjusted. This would effectively allow scaling the simulated SIF time series shown in Figs. 9, 10 and 11. Similarly, the parameters in the empirical observation operator for VOD would also be included in the set of parameters to be adjusted in assimilation mode. We also note that many of the model's parameters are not very well constrained, and could therefore change substantially. For example, an adjustment of the turnover times for the litter and soil organic matter pools will change heterotrophic respiration, and according to SI Equ. 153 the fit to simulated TER shown in Figure 3 and Figure 6. This could happen in the framework of either a local-scale assimilation of eddy flux measurements as used here for evaluation, or on a regional to global scale with the assimilation of atmospheric $CO_2$ data, including those from space-based remote sensing (Buchwitz et al., 2017).

A further limitation we found is that the model overestimates soil water limitation at the savannah site. This may be linked to the parameterisation of soil hydrological properties, or to the parameterisation of rooting depth and root penetration of the
540   soil, both of which warrant further investigation.

A principal advantage of the process-based modelling approach presented here is that the system can be used to identify, better investigate and quantify specific processes – a fundamental and often decisive advantage over machine learning, or complex statistical modelling systems (Thessen, 2016; Lary et al., 2018). The advantage translates into a principal limitation in that if a given process contributes to the measured signal, it has to be represented. Otherwise, missing process representation
545   can lead to misleading parameter choices that use processes included within the system to compensate for the missing process – also known as "matching observations for the wrong reasons". Therefore, process modelling requires significant expert knowledge on ecosystem functioning as well as experience with or direct contact to experimental teams, compared to statistical interference methods, including machine learning.

## 6.4   Outlook

550   In this study, we have shown the value of the four data streams (FAPAR, SIF, VOD and surface soil moisture), as opposed to the intrinsically local measurements used for the initial evaluation, which lies in their availability over large spatial scales. Therefore, such data streams derived from Earth Observation sources will make it possible to evaluate the model across larger, regional scales. The immediately next step would therefore be to evaluate D&B with regional rather than local observations and see if in such a set-up the noted model-observation differences are reduced. The advantage of regional comparisons is
555   that substantial uncertainties arising from small-scale conditions are averaged out, and the scale of comparison may by more appropriate for a typical application of the model.

At such a regional scale, it will further be possible to assimilate those data streams using the principle setup described above. Here, it will be possible to either adjust parameters spatially grouped by PFT, following CCDAS (Kaminski et al., 2013), or independently at each pixel following DALEC (Quaife et al., 2007). A further approach that has not yet been tested would
560   be a combination of the two, where parameters are adjusted at every grid cell independently, but with a partial constraint on parameter values assuming that those values co-vary depending on closeness of geographical location, altitude, land use, PFT, or soil type.

A significant advantage of such a data assimilation system will be the possibility to investigate if the process model is capable of matching the observations not only for specific parameter set, but within reasonable bounds of the entire model-
565   parameter space. Only if that is not possible can we rigorously conclude that the remaining model-observation mismatch is caused by missing processes. We consider such investigations the next logical step of development of the D&B modelling system, besides any inclusion of further Earth Observation data streams. The further goal would then be to apply it to the task of routinely producing data products on carbon and energy fluxes.

*Code and data availability.* The D&B code in Fortran90 is hosted, with simulation results, at the Zenodo repository under the AGPL li-
570 cense, available through https://zenodo.org/doi/10.5281/zenodo.11243753 and will also be available, with updates, from its repository via
https://gitlab.gwdg.de/tccas-team/TCCAS.git. The observations are available on the TCCAS home page https://tccas.inversion-lab.com/database.html
and have been permanently archived at https://zenodo.org/doi/10.5281/zenodo.12725764

*Author contributions.* WK drafted and finalized manuscript. MD developed the layout of the activity combining modelling, field work and
EO. WK and MD provided original model design and description of D&B. WK, MW, TK, MV, TLS, MS, TG, TT, TLQ, SZ further designed
575 and validated D&B. TK, MV, and WK implemented D&B and integrated module for carbon balance and phenology. MV and TK performed
model simulations. AK, JL, MA, MH, TG, TSeM provided field data. MV, AO, and TM prepared data and plots. TLS and MW drafted
sections on carbon balance and phenology and provided module for carbon balance and phenology. TLQ drafted sections on SIF observation
operator. All authors contributed to the discussions on analysis of results or commented on or edited manuscript.

*Competing interests.* At least one of the (co-)authors is a member of the editorial board of Geoscientific Model Development.

580 *Acknowledgements.* This work was funded by ESA through contracts 4000131497 (LCC study) and 4000141232 (TCCAS study) within
the Carbon Science Cluster and by the European Union's Horizon Europe Programme through Grant Agreement 101082194. T. Thum and
T. Miinalainen were funded by the Research Council of Finland (grant number 330165). Y. H. Kerr was funded by the Centre National
d'Etudes Spatiales through the Terre Ocean Surface Continentales Atmosphere (TOSCA) programme. T. S. El-Madany thanks the Alexander
von Humboldt Stiftung for financial support of the MaNiP project and Arnaud Carrara, Ramon Lopez-Jiminez, Gerardo Moreno, Victor
585 Rolo, and M. Pilar Martín and her SpecLab team for support of fieldwork. J.Verelst and P. Reyez-Muñoz were funded by the European Union
(ERC, FLEXINEL, 101086622). Views and opinions expressed are however those of the author(s) only and do not necessarily reflect those
of the European Union or the European Research Council. Neither the European Union nor the granting authority can be held responsible
for them.

# References

590    Arora, V. K., Katavouta, A., Williams, R. G., Jones, C. D., Brovkin, V., Friedlingstein, P., Schwinger, J., Bopp, L., Boucher, O., Cadule, P.,
      et al.: Carbon–concentration and carbon–climate feedbacks in CMIP6 models and their comparison to CMIP5 models, Biogeosciences,
      17, 4173–4222, 2020.

      Babaeian, E., Sadeghi, M., Jones, S. B., Montzka, C., Vereecken, H., and Tuller, M.: Ground, proximal, and satellite remote sensing of soil
      moisture, Reviews of Geophysics, 57, 530–616, 2019.

595    Berger, M., Moreno, J., Johannessen, J. A., Levelt, P. F., and Hanssen, R. F.: ESA's sentinel missions in support of Earth system science,
      Remote Sensing of Environment, 120, 84–90, 2012.

      Bloom, A. A. and Williams, M.: Constraining ecosystem carbon dynamics in a data-limited world: Integrating ecological "common sense"
      in a model-data fusion framework, Biogeosciences, 12, 1299–1315, https://doi.org/10.5194/bg-12-1299-2015, 2015.

      Buchwitz, M., Reuter, M., Schneising, O., Hewson, W., Detmers, R. G., Boesch, H., Hasekamp, O. P., Aben, I., Bovensmann, H., Burrows,
600    J. P., et al.: Global satellite observations of column-averaged carbon dioxide and methane: The GHG-CCI XCO2 and XCH4 CRDP3 data
      set, Remote Sensing of Environment, 203, 276–295, 2017.

      Ciais, P., Dolman, A. J., Bombelli, A., Duren, R., Peregon, A., Rayner, P. J., Miller, C., Gobron, N., Kinderman, G., Marland, G., et al.:
      Current systematic carbon-cycle observations and the need for implementing a policy-relevant carbon observing system, Biogeosciences,
      11, 3547–3602, 2014.

605    Disney, M., Muller, J.-P., Kharbouche, S., Kaminski, T., Voßbeck, M., Lewis, P., and Pinty, B.: A new global fAPAR and LAI dataset derived
      from optimal albedo estimates: Comparison with MODIS products, Remote Sensing, 8, 275, 2016.

      El-Madany, T. S., Reichstein, M., Perez-Priego, O., Carrara, A., Moreno, G., Martín, M. P., Pacheco-Labrador, J., Wohlfahrt, G., Nieto,
      H., Weber, U., et al.: Drivers of spatio-temporal variability of carbon dioxide and energy fluxes in a Mediterranean savanna ecosystem,
      Agricultural and Forest Meteorology, 262, 258–278, 2018.

610    Famiglietti, C. A., Smallman, T. L., Levine, P. A., Flack-Prain, S., Quetin, G. R., Meyer, V., and et al.: Optimal model complexity for
      terrestrial carbon cycle prediction, Journal of Advances in Modeling Earth Systems, 18, 2727–2754, https://doi.org/10.5194/bg-18-2727-
      2021, 2021.

      Farquhar, G., von Caemmerer, S. v., and Berry, J.: A biochemical model of photosynthetic CO2 assimilation in leaves of C3 species, Planta,
      149, 78–90, 1980.

615    Friedlingstein, P., O'sullivan, M., Jones, M. W., Andrew, R. M., Gregor, L., Hauck, J., Le Quéré, C., Luijkx, I. T., Olsen, A., Peters, G. P.,
      et al.: Global carbon budget 2022, Earth System Science Data, 14, 4811–4900, 2022.

      Gao, H., Liu, S., Lu, W., Smith, A. R., Valbuena, R., Yan, W., Wang, Z., Xiao, L., Peng, X., Li, Q., et al.: Global analysis of the relationship
      between reconstructed solar-induced chlorophyll fluorescence (SIF) and gross primary production (GPP), Remote Sensing, 13, 2824,
      2021.

620    Gerten, D., Hoff, H., Bondeau, A., Lucht, W., Smith, P., and Zaehle, S.: Contemporary "green" water flows: Simulations with a dynamic
      global vegetation and water balance model, Physics and Chemistry of the Earth, Parts A/B/C, 30, 334–338, 2005.

      Gu, L., Han, J., Wood, J. D., Chang, C. Y.-Y., and Sun, Y.: Sun-induced Chl fluorescence and its importance for biophysical modeling of
      photosynthesis based on light reactions, New Phytologist, 223, 1179–1191, 2019.

      Heiskanen, J., Brümmer, C., Buchmann, N., Calfapietra, C., Chen, H., Gielen, B., Gkritzalis, T., Hammer, S., Hartman, S., Herbst, M., et al.:
625    The integrated carbon observation system in Europe, Bulletin of the American Meteorological Society, 103, E855–E872, 2022.

Helmisaari, H.-S., Makkonen, K., Kellomäki, S., Valtonen, E., and Mälkönen, E.: Below-and above-ground biomass, production and nitrogen use in Scots pine stands in eastern Finland, Forest ecology and management, 165, 317–326, 2002.

Honkanen, M., Heikkinen, P., MacArthur, A., Thum, T., Kivi, R., and Lindqvist, H.: UAV-Borne Measurements of Solar-Induced Chlorophyll Fluorescence (SIF) at a Boreal Site, in: International conference on FinDrones, pp. 115–135, Springer, 2023.

630   Jarvis, P. G. and McNaughton, K.: Stomatal control of transpiration: scaling up from leaf to region, Advances in Ecological Research, 15, 1–49, 1986.

Kaminski, T. and Mathieu, P.-P.: Reviews and syntheses: Flying the satellite into your model: on the role of observation operators in constraining models of the Earth system and the carbon cycle, Biogeosciences, 14, 2343–2357, https://doi.org/10.5194/bg-14-2343-2017, 2017.

635   Kaminski, T., Knorr, W., Scholze, M., Gobron, N., Pinty, B., Giering, R., and Mathieu, P.-P.: Consistent assimilation of MERIS FA-PAR and atmospheric $CO_2$ into a terrestrial vegetation model and interactive mission benefit analysis, Biogeosciences, 9, 3173–3184, https://doi.org/10.5194/bg-9-3173-2012, 2012.

Kaminski, T., Knorr, W., Schürmann, G., Scholze, M., Rayner, P. J., Zaehle, S., Blessing, S., Dorigo, W., Gayler, V., Giering, R., Gobron, N., Grant, J. P., Heimann, M., Hooker-Strout, A., Houweling, S., Kato, T., Kattge, J., Kelley, D., Kemp, S., Koffi, E. N., Köstler, C., Mathieu,
640   P., Pinty, B., Reick, C. H., Rödenbeck, C., Schnur, R., Scipal, K., Sebald, C., Stacke, T., van Scheltinga, A. T., Vossbeck, M., Widmann, H., and Ziehn, T.: The BETHY/JSBACH Carbon Cycle Data Assimilation System: experiences and challenges, J. Geophys. Res., 118, doi:10.1002/jgrg.20 118, http://onlinelibrary.wiley.com/doi/10.1002/jgrg.20118/abstract, 2013.

Kerr, Y., Waldteufel, P., Wigneron, J.-P., Delwart, S., Cabot, F., Boutin, J., Escorihuela, M.-J., Font, J., Reul, N., Gruhier, C., Juglea, S., Drinkwater, M., Hahne, A., Martin-Neira, M., and Mecklenburg, S.: The SMOS Mission: New Tool for Monitoring Key Elements ofthe
645   Global Water Cycle, Proceedings of the IEEE, 98, 666–687, https://doi.org/10.1109/JPROC.2010.2043032, 2010.

Kerr, Y. H., Waldteufel, P., Richaume, P., Wigneron, J. P., Ferrazzoli, P., Mahmoodi, A., Al Bitar, A., Cabot, F., Gruhier, C., Juglea, S. E., et al.: The SMOS soil moisture retrieval algorithm, IEEE transactions on geoscience and remote sensing, 50, 1384–1403, 2012.

Kirdiashev, K., Chukhlantsev, A., and Shutko, A.: Microwave radiation of the earth's surface in the presence of vegetation cover, Radiotekhnika i Elektronika, 24, 256–264, 1979.

650   Knorr, W.: Satellitengestützte Fernerkundung und Modellierung des Globalen $CO_2$ -Austauschs der Landvegetation: Eine Synthese, Ph.D. thesis, Max-Planck-Institut für Meteorologie, Hamburg, Germany, 1997.

Knorr, W.: Annual And Interannual $CO_2$ Exchanges Of The Terrestrial Biosphere: Process-Based Simulations And Uncertainties, Glob. Ecol. Biogeogr., 9, 225–252, 2000.

Knorr, W. and Kattge, J.: Inversion of terrestrial biosphere model parameter values against eddy covariance measurements using Monte Carlo
655   sampling, Global Change Biology, 11, 1333–1351, 2005.

Knorr, W. and Lakshmi, V.: Assimilationof fAPAR and Surface Temperature Into a Land Surface and Vegetation Model, in: Land Surface Hydrology, Meteorology, and Climate: Observations and Modeling, edited by Lakshmi, V., Albertson, J., and Schaake, J., pp. 177 – 200, American Geophysical Union, ISBN 0875903525, 2001.

Knorr, W., Kaminski, T., Scholze, M., Gobron, N., Pinty, B., Giering, R., and Mathieu, P.-P.: Carbon cycle data assimilation with a generic
660   phenology model, J. Geophys. Res., 115, https://doi.org/10.1029/2009JG001119, 2010.

Konings, A. G., Rao, K., and Steele-Dunne, S. C.: Macro to micro: microwave remote sensing of plant water content for physiology and ecology, New Phytologist, 223, 1166–1172, https://doi.org/https://doi.org/10.1111/nph.15808, _eprint: https://nph.onlinelibrary.wiley.com/doi/pdf/10.1111/nph.15808, 2019.

Lary, D. J., Zewdie, G. K., Liu, X., Wu, D., Levetin, E., Allee, R. J., Malakar, N., Walker, A., Mussa, H., Mannino, A., et al.: Machine
665    learning applications for earth observation, Earth observation open science and innovation, 165, 2018.

Lin, J., Zhou, L., Wu, J., Han, X., Zhao, B., Chen, M., and Liu, L.: Water stress significantly affects the diurnal variation of solar-induced
chlorophyll fluorescence (SIF): A case study for winter wheat, Science of The Total Environment, 908, 168 256, 2024.

Liu, Z., Zhao, F., Liu, X., Yu, Q., Wang, Y., Peng, X., Cai, H., and Lu, X.: Direct estimation of photosynthetic CO2 assimilation from
solar-induced chlorophyll fluorescence (SIF), Remote Sensing of Environment, 271, 112 893, 2022.

670    Loth, B. and Graf, H.: Modelling the snow cover for climate studies, Tech. Rep. 190, Max-Planck-Institut für Meteorologie, Hamburg,
Germany, 1996.

Magney, T. S., Frankenberg, C., Köhler, P., North, G., Davis, T. S., Dold, C., Dutta, D., Fisher, J. B., Grossmann, K., Harring-
ton, A., Hatfield, J., Stutz, J., Sun, Y., and Porcar-Castell, A.: Disentangling Changes in the Spectral Shape of Chlorophyll Fluo-
rescence: Implications for Remote Sensing of Photosynthesis, Journal of Geophysical Research: Biogeosciences, 124, 1491–1507,
675    https://doi.org/https://doi.org/10.1029/2019JG005029, 2019.

Mo, T., Choudhury, B. J., Schmugge, T. J., Wang, J. R., and Jackson, T. J.: A model for microwave emission from vegetation-covered fields,
Journal of Geophysical Research: Oceans, 87, 11 229–11 237, https://doi.org/https://doi.org/10.1029/JC087iC13p11229, 1982.

Mohammed, G. H., Colombo, R., Middleton, E. M., Rascher, U., van der Tol, C., Nedbal, L., Goulas, Y., Pérez-Priego, O., Damm, A.,
Meroni, M., et al.: Remote sensing of solar-induced chlorophyll fluorescence (SIF) in vegetation: 50 years of progress, Remote sensing of
680    environment, 231, 111 177, 2019.

Nair, R. K., Morris, K. A., Migliavacca, M., Moreno, G., and Schrumpf, M.: Plant-available N: P alters root litter N recycling in a Mediter-
ranean tree–grass ecosystem, Journal of Plant Nutrition and Soil Science, 183, 517–529, 2020.

NOAA: Trends in Atmospheric Carbon Dioxide, Global Monitoring Laboratory, https://gml.noaa.gov/webdata/ccgg/trends/co2/co2_
annmean_mlo.txt, accessed 1 Feb 2024, 2024.

685    Norton, A. J., Rayner, P. J., Koffi, E. N., and Scholze, M.: Assimilating solar-induced chlorophyll fluorescence into the terrestrial bio-
sphere model BETHY-SCOPE: Model description and information content, Geoscientific Model Development Discussions, 2017, 1–26,
https://doi.org/10.5194/gmd-2017-34, 2017.

Norton, A. J., Rayner, P. J., Koffi, E. N., and Scholze, M.: Assimilating solar-induced chlorophyll fluorescence into the terrestrial bio-
sphere model BETHY-SCOPE v1.0: model description and information content, Geoscientific Model Development, 11, 1517–1536,
690    https://doi.org/10.5194/gmd-11-1517-2018, 2018.

Norton, A. J., Rayner, P. J., Koffi, E. N., Scholze, M., Silver, J. D., and Wang, Y.-P.: Estimating global gross primary productiv-
ity using chlorophyll fluorescence and a data assimilation system with the BETHY-SCOPE model, Biogeosciences, 16, 3069–3093,
https://doi.org/10.5194/bg-16-3069-2019, 2019.

Porcar-Castell, A., Tyystjärvi, E., Atherton, J., Van der Tol, C., Flexas, J., Pfündel, E. E., Moreno, J., Frankenberg, C., and Berry, J. A.:
695    Linking chlorophyll a fluorescence to photosynthesis for remote sensing applications: mechanisms and challenges, Journal of experimental
botany, 65, 4065–4095, 2014.

Quaife, T., Lewis, P., Disney, M., De Kauwe, M., Williams, M., and Law, B.: Assimilating reflectance data into a ecosystem model to
improve estimates of terrestrial carbon flux, in: 10th International Symposium on Physical Measurements and Signatures in Remote
Sensing, publisher Copyright: © 2007 International Society for Photogrammetry and Remote Sensing. All rights reserved., 2007.

700    Quegan, S., Le Toan, T., Chave, J., Dall, J., Exbrayat, J.-F., Minh, D. H. T., Lomas, M., D'Alessandro, M. M., Paillou, P., Papathanassiou,
K., Rocca, F., Saatchi, S., Scipal, K., Shugart, H., Smallman, T. L., Soja, M. J., Tebaldini, S., Ulander, L., Villard, L., and Williams, M.:

The European Space Agency BIOMASS mission: Measuring forest above-ground biomass from space, Remote Sensing of Environment, 227, 44–60, https://doi.org/https://doi.org/10.1016/j.rse.2019.03.032, 2019.

Rayner, P., Scholze, M., Knorr, W., Kaminski, T., Giering, R., and Widmann, H.: Two decades of terrestrial Carbon fluxes from a Carbon Cycle Data Assimilation System (CCDAS), Global Biogeochemical Cycles, 19, doi:10.1029/2004GB002 254, 2005.

Rebmann, C., Aubinet, M., Schmid, H., Arriga, N., Aurela, M., Burba, G., Clement, R., De Ligne, A., Fratini, G., Gielen, B., et al.: ICOS eddy covariance flux-station site setup: a review, International Agrophysics, 32, 471–494, 2018.

Running, S. W. and Zhao, M.: Daily GPP and annual NPP (MOD17A2/A3) products NASA Earth Observing System MODIS land algorithm, MOD17 User's Guide, 2015, 1–28, 2015.

Scholze, M., Kaminski, T., Knorr, W., Blessing, S., Vossbeck, M., Grant, J., and Scipal, K.: Simultaneous assimilation of SMOS soil moisture and atmospheric $CO_2$ in-situ observations to constrain the global terrestrial carbon cycle, Remote Sensing of Environment, 180, 334–345, 2016.

Scholze, M., Buchwitz, M., Dorigo, W., Guanter, L., and Quegan, S.: Reviews and syntheses: Systematic Earth observations for use in terrestrial carbon cycle data assimilation systems, Biogeosciences, 14, 3401–3429, 2017.

Scholze, M., Kaminski, T., Knorr, W., Voßbeck, M., Wu, M., Ferrazzoli, P., Kerr, Y., Mialon, A., Richaume, P., Rodríguez-Fernández, N., Vittucci, C., Wigneron, J.-P., Mecklenburg, S., and Drusch, M.: Mean European Carbon Sink Over 2010-2015 Estimated by Simultaneous Assimilation of Atmospheric CO2, Soil Moisture, and Vegetation Optical Depth, Geophysical Research Letters, 46, 13 796–13 803, https://doi.org/10.1029/2019GL085725, 2019.

Schwank, M., Kontu, A., Mialon, A., Naderpour, R., Houtz, D., Lemmetyinen, J., Rautiainen, K., Li, Q., Richaume, P., Kerr, Y., and Mätzler, C.: Temperature effects on L-band vegetation optical depth of a boreal forest, Remote Sensing of Environment, 263, 112 542, https://doi.org/https://doi.org/10.1016/j.rse.2021.112542, 2021.

Sellers, P. J.: Canopy reflectance, photosynthesis and transpiration, International Journal of Remote Sensing, 6, 1335–1372, https://doi.org/10.1080/01431168508948283, 1985.

Smallman, T. L., Exbrayat, J.-F., Mencuccini, M., Bloom, A. A., and Williams, M.: Assimilation of repeated woody biomass observations constrains decadal ecosystem carbon cycle uncertainty in aggrading forests, Journal of Geophysical Research: Biogeosciences, 122, 528–545, https://doi.org/https://doi.org/10.1002/2016JG003520, 2017.

Smith, B., Prentice, I. C., and Sykes, M. T.: Representation of vegetation dynamics in the modelling of terrestrial ecosystems: comparing two contrasting approaches within European climate space, Global ecology and biogeography, pp. 621–637, 2001.

Thessen, A.: Adoption of machine learning techniques in ecology and earth science, One Ecosystem, 1, e8621, 2016.

Thum, T., Aalto, T., Laurila, T., Aurela, M., Kolari, P., and Hari, P.: Parametrization of two photosynthesis models at the canopy scale in a northern boreal Scots pine forest, Tellus B: Chemical and Physical Meteorology, 59, 874–890, 2007.

Ulaby, F. T. and Wilson, E. A.: Microwave attenuation properties of vegetation canopies, IEEE Transactions on Geoscience and Remote Sensing, pp. 746–753, 1985.

Wang, J., Xiao, X., Wagle, P., Ma, S., Baldocchi, D., Carrara, A., Zhang, Y., Dong, J., and Qin, Y.: Canopy and climate controls of gross primary production of Mediterranean-type deciduous and evergreen oak savannas, Agricultural and forest meteorology, 226, 132–147, 2016.

Wigneron, J.-P., Kerr, Y., Waldteufel, P., Saleh, K., Escorihuela, M.-J., Richaume, P., Ferrazzoli, P., de Rosnay, P., Gurney, R., Calvet, J.-C., Grant, J., Guglielmetti, M., Hornbuckle, B., Mätzler, C., Pellarin, T., and Schwank, M.: L-band Microwave Emission of the Biosphere (L-

MEB) Model: Description and calibration against experimental data sets over crop fields, Remote Sensing of Environment, 107, 639–655,
740 https://doi.org/https://doi.org/10.1016/j.rse.2006.10.014, 2007.

Wigneron, J.-P., Chanzy, A., Kerr, Y. H., Lawrence, H., Shi, J., Escorihuela, M. J., Mironov, V., Mialon, A., Demontoux, F., De Rosnay, P.,
et al.: Evaluating an improved parameterization of the soil emission in L-MEB, IEEE Transactions on Geoscience and Remote Sensing,
49, 1177–1189, 2010.

Williams, M., Schwarz, P. A., Law, B. E., Irvine, J., and Kurpius, M. R.: An improved analysis of forest carbon dynamics using data
745 assimilation, Global Change Biology, 11, 89–105, 2005.

Wood, E., Lettenmaier, D., and Zartarian, V.: A land-surface hydrology parameterization with subgrid variability for general circulation
models, J. Geophys. Res., 97, 2717–2728, 1992.

Zobler, L.: A World Soil File for Global Climate Modelling, NASA Tech. memo 87802, 32, 1986.
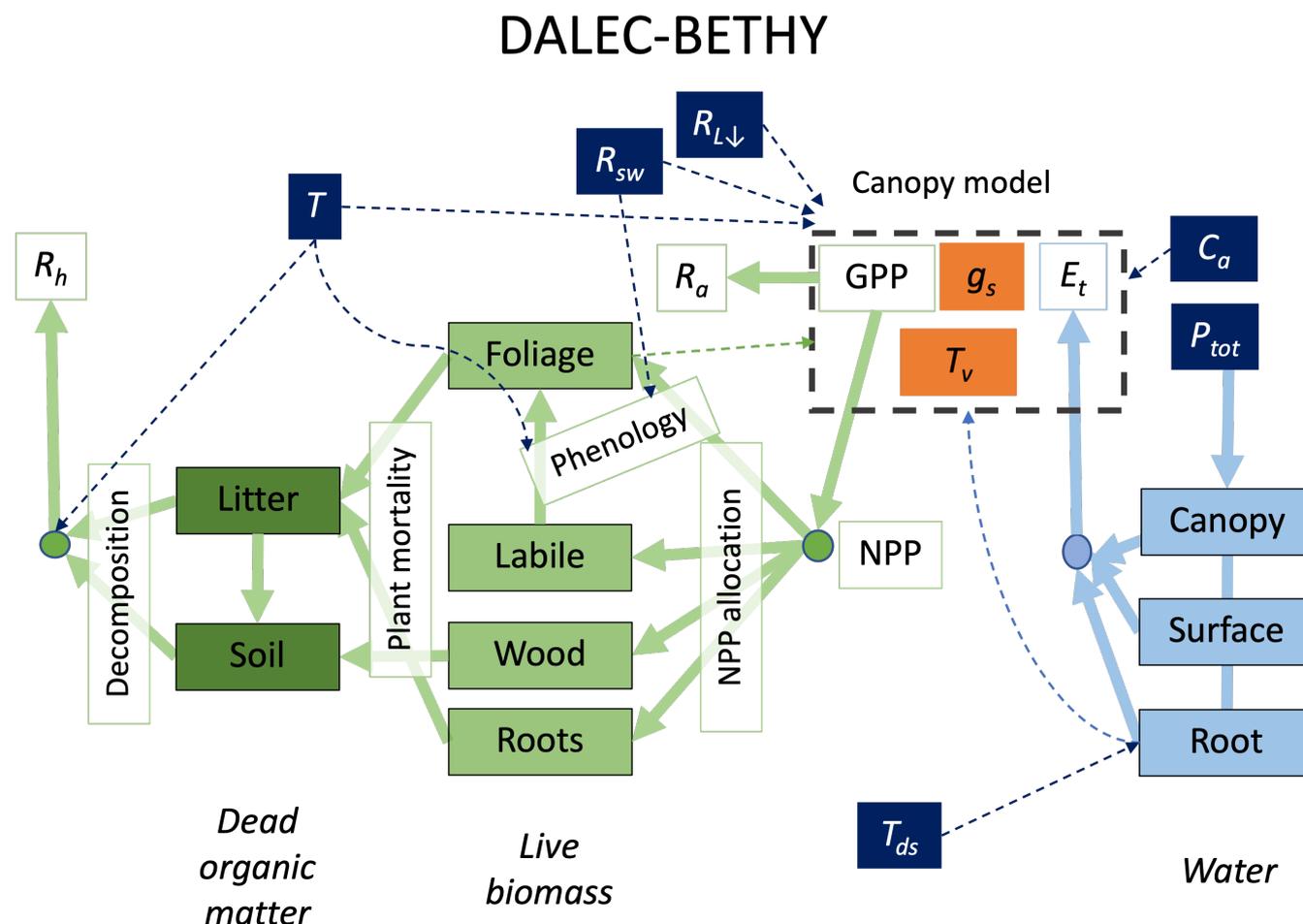
# DALEC-BETHY

**Figure 1.** Structure of the DALEC-BETHY coupled model. State variables are in filled boxes; green for carbon, pale blue for water, orange for canopy states of stomatal conductance ($g_s$) and leaf temperature ($T_v$). Drivers are shown with white text in dark blue boxes ($T$: air temperature, $T_{ds}$: deep-soil temperature, $R_{sw}$: downwelling shortwave radiation, $R_{L\downarrow}$: downwelling longwave radiation; $P_{tot}$: total precipitation, $C_a$: CO$_2$ concentration in air). Fluxes are shown as solid arrows and annotated by open boxes; coloured green for C fluxes and pale blue for water. GPP is gross primary production; NPP is net primary production; $R_A$ is autotrophic respiration; $R_H$ is heterotrophic respiration; $E_t$ is evapotranspiration. Dashed arrows show influences – for example $T$ and $R_{sw}$ influence the modelling of phenology.
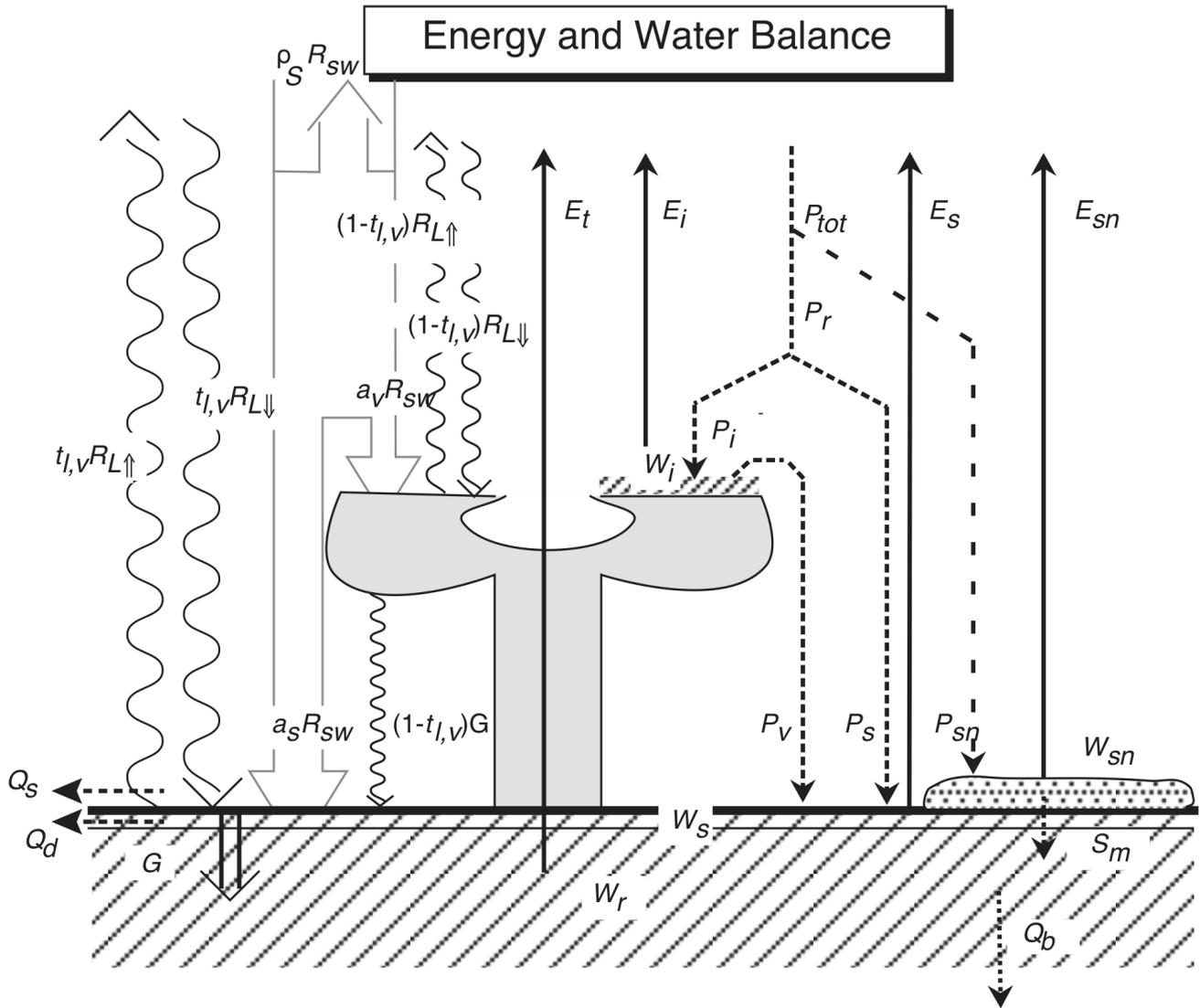
**Figure 2.** Energy and water balance of the D&B model with symbols for fluxes (normal) and reservoirs (italics). $a_s$: soil absorption of shortwave radiation, $a_v$: canopy absorption of shortwave radiation, $E_i$: intercepted-water (canopy) evaporation, $E_s$: soil evaporation; $E_{sn}$: snow evaporation, $E_t$: transpiration, $G$: ground heat flux, $P_i$: intercepted rainfall; $P_r$: rainfall; $P_s$ rainfall on soil; $P_{sn}$: snowfall, $P_{tot}$: total precipitation; $P_v$: throughfall, $Q_b$: baseflow, $Q_d$: horizontal drainage, $Q_s$: surface runoff, $R_{L,\uparrow}$: upwelling longwave radiation, $R_{L,\downarrow}$: downwelling longwave radiation, $R_{sw}$: downwelling shortwave radiation, $t_{l,v}$: longwave canopy transmission, $W_i$: intercepted water amount, $W_r$: root-zone soil moisture, $W_s$: surface-layer soil moisture, $W_{sn}$: snow amount, $\rho_S$: surface reflectance.
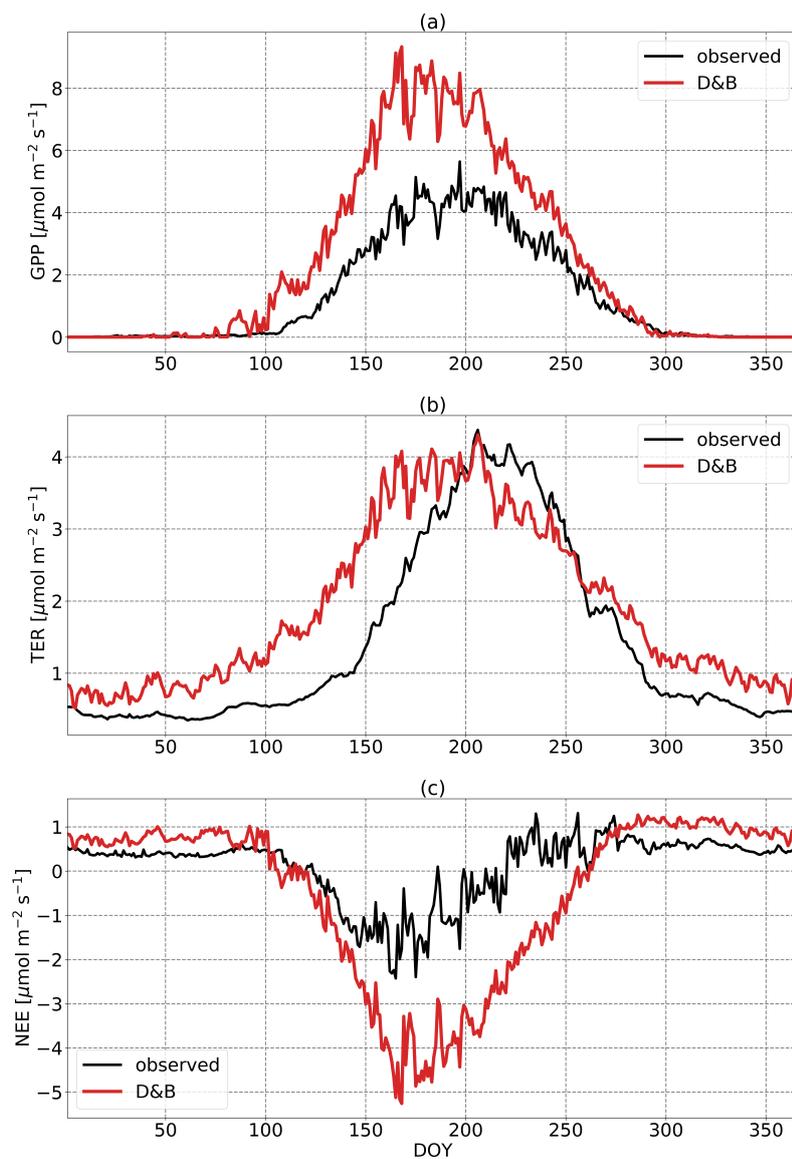
**Figure 3.** Annual cycles of daily (a) GPP, (b) TER, and (c) NEE at Sodankylä, averaged over the years 2016 to 2021. Black line is observation based on eddy-covariance data, the red line D&B.
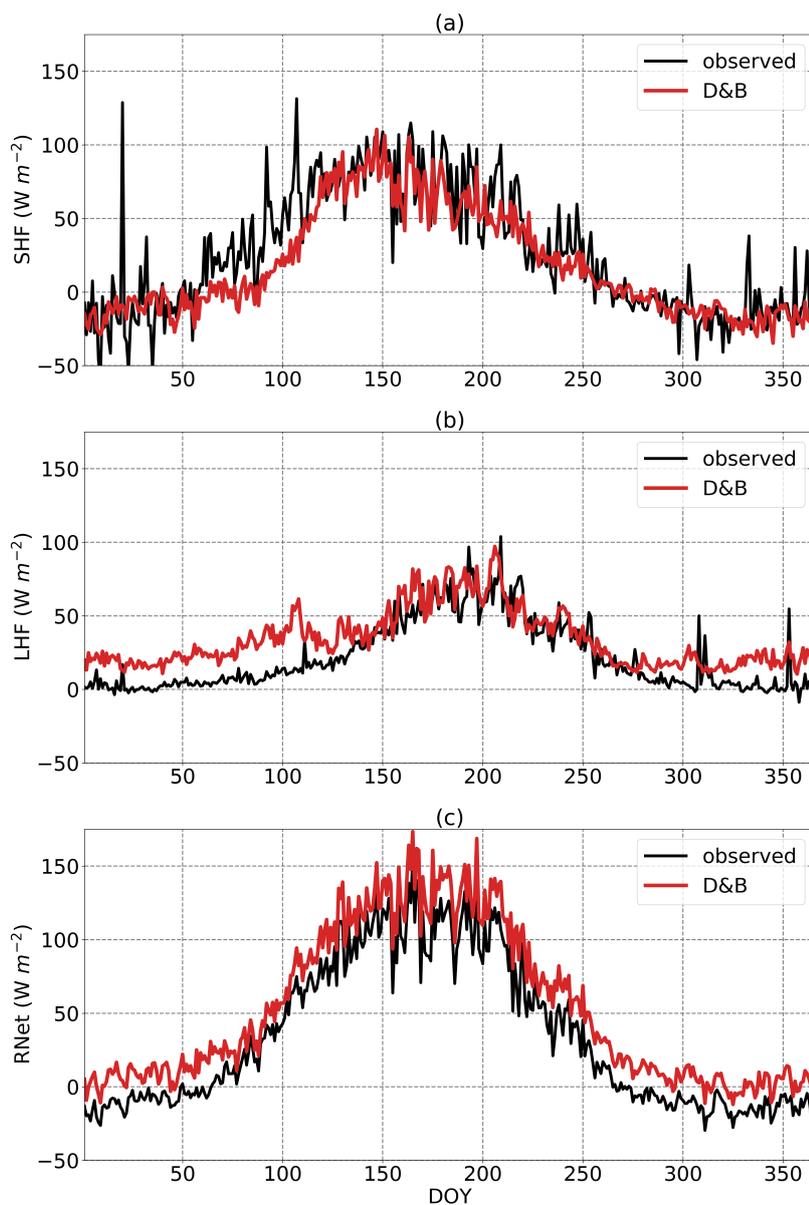
**Figure 4.** Annual cycles of daily (a) sensible heat flux, (b) latent heat flux, and (c) net radiation minus ground heat flux at Sodankylä, averaged over the years 2016 to 2021.
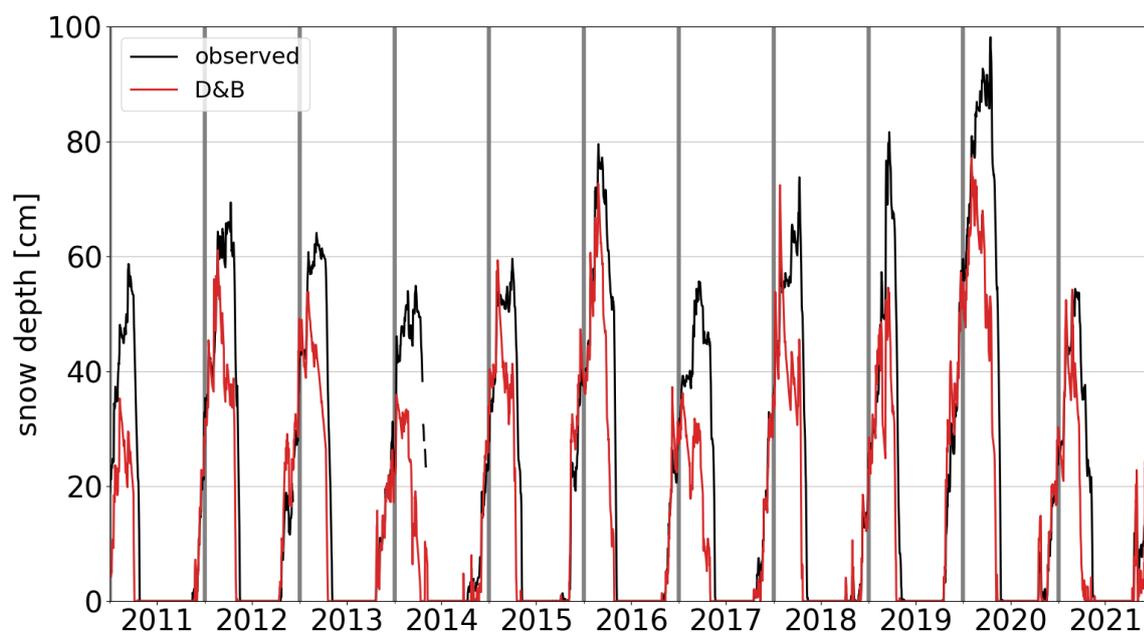
**Figure 5.** Daily observed (black) and simulated (red) snow depth at Sodankylä for the years 2011-2021. Simulated snow depth is for the evergreen conifer PFT only.
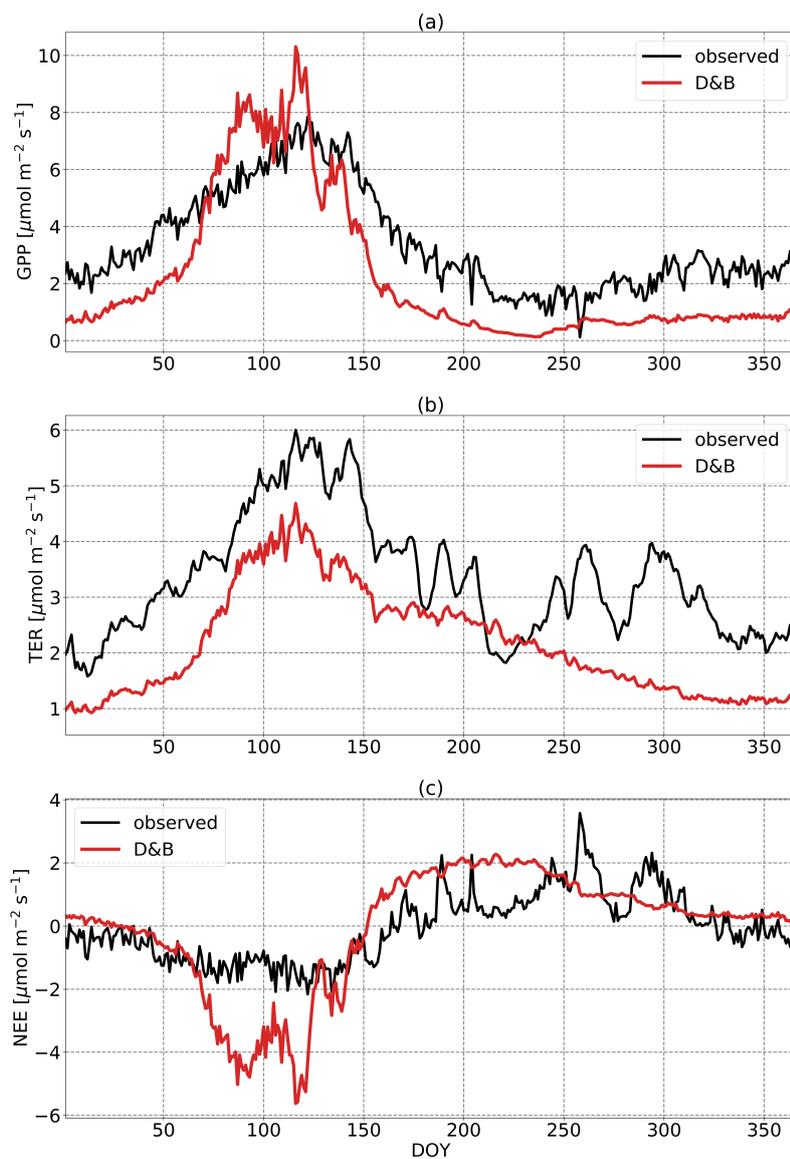
**Figure 6.** Annual cycles of daily (a) GPP, (b) TER, and (c) NEE at Majadas de Tietar, averaged over the years 2016 to 2021. Black line is observation based on eddy-covariance data, the red line D&B.
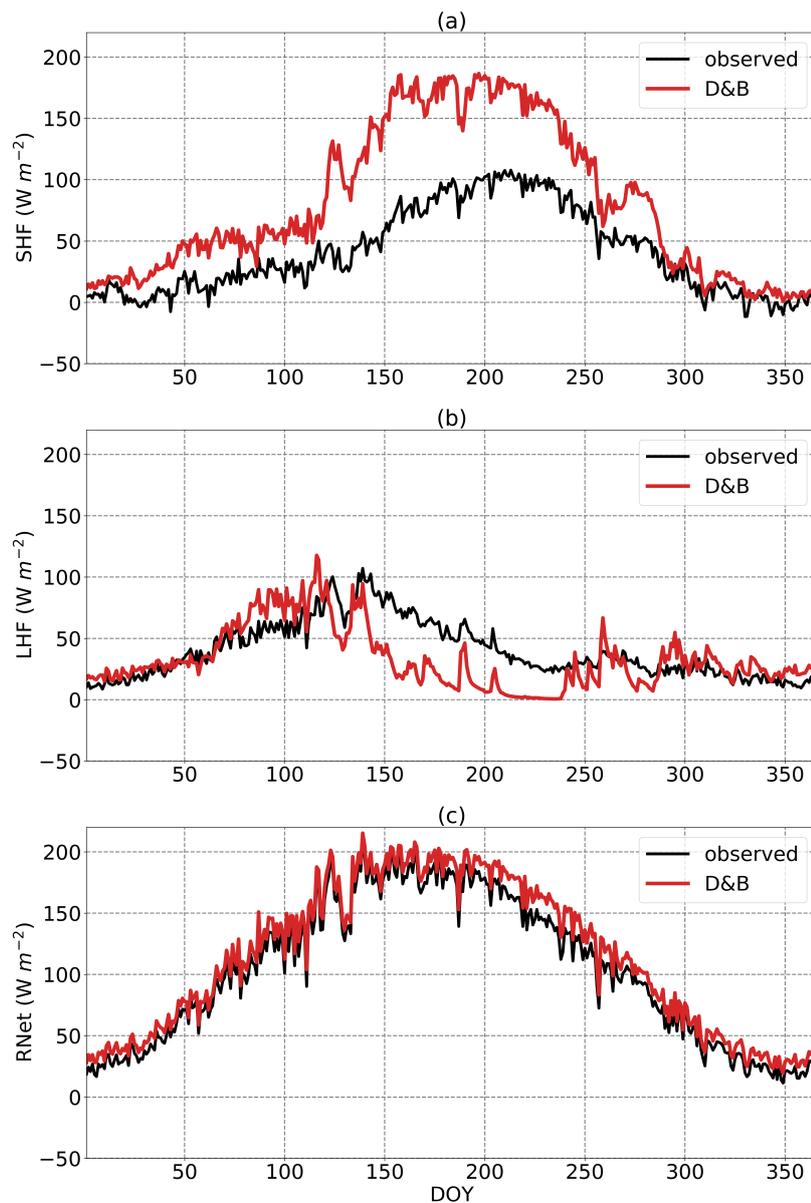
**Figure 7.** Annual cycles of daily (a) sensible heat flux, (b) latent heat flux, and (c) net radiation minus ground heat flux at Majadas de Tietar, averaged over the years 2016 to 2021.
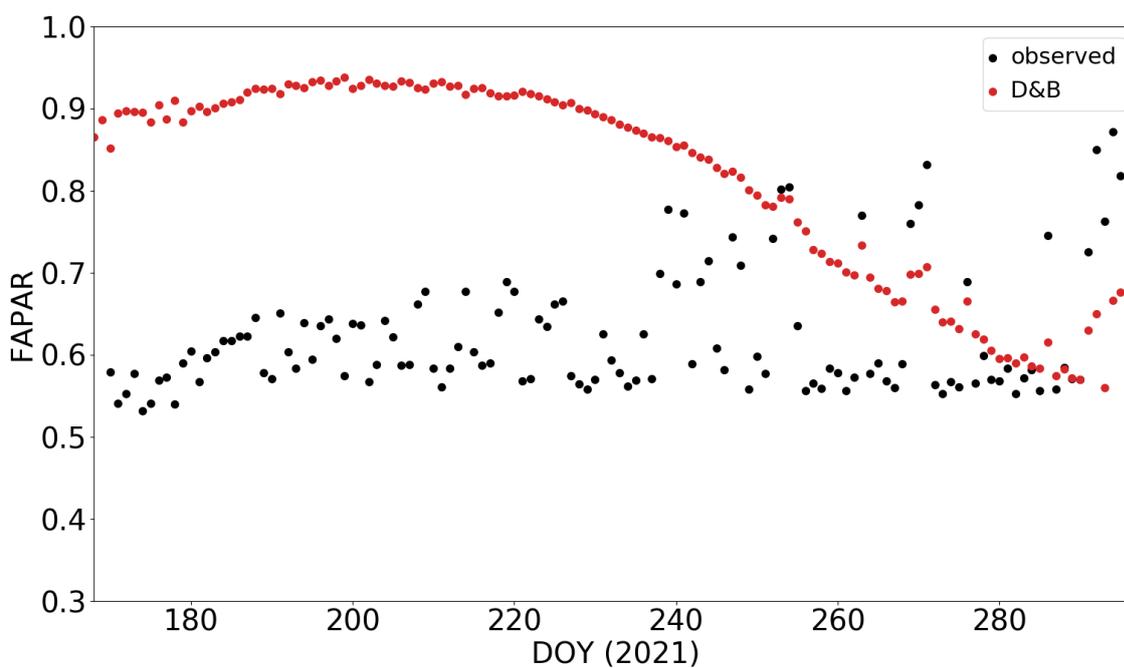
**Figure 8.** Observed (black) and simulated (red) FAPAR at Sodankylä between 19 June and 22 October 2021. Simulated FAPAR is for the evergreen conifer PFT only, in accordance with the vegetation within the field of view of the FAPAR sensor.
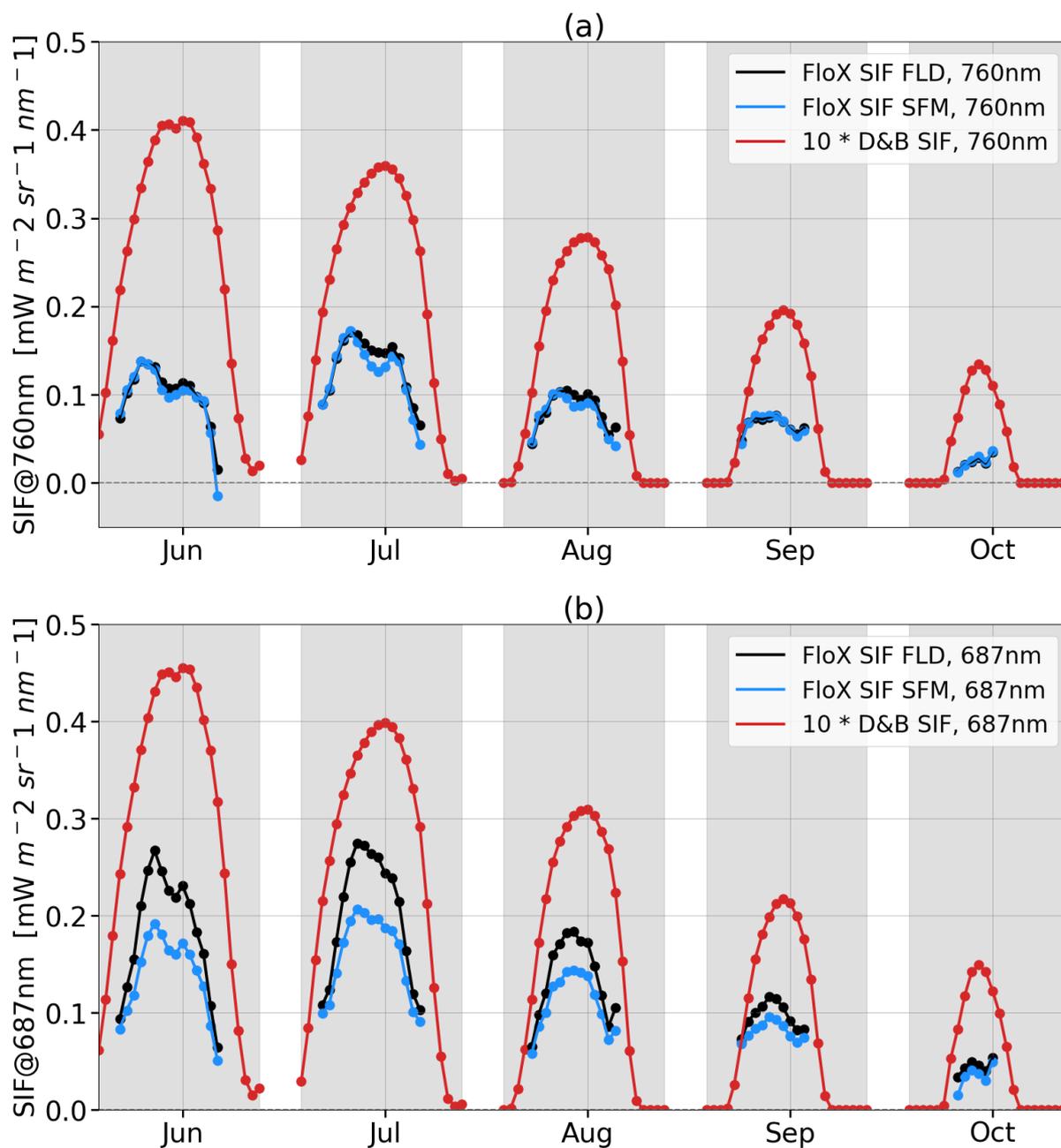
**Figure 9.** Average diurnal cycle by month of far-red (a) and red SIF (b) for pine forest (PFT 5) at Sodankylä for months June to October in 2021. D&B simulations (red) against measurements with the Fluorescence Box (FloX): retrievals made with the Frauenhofer line discrimination (black) and retrieval made with the spectral fitting method (blue).
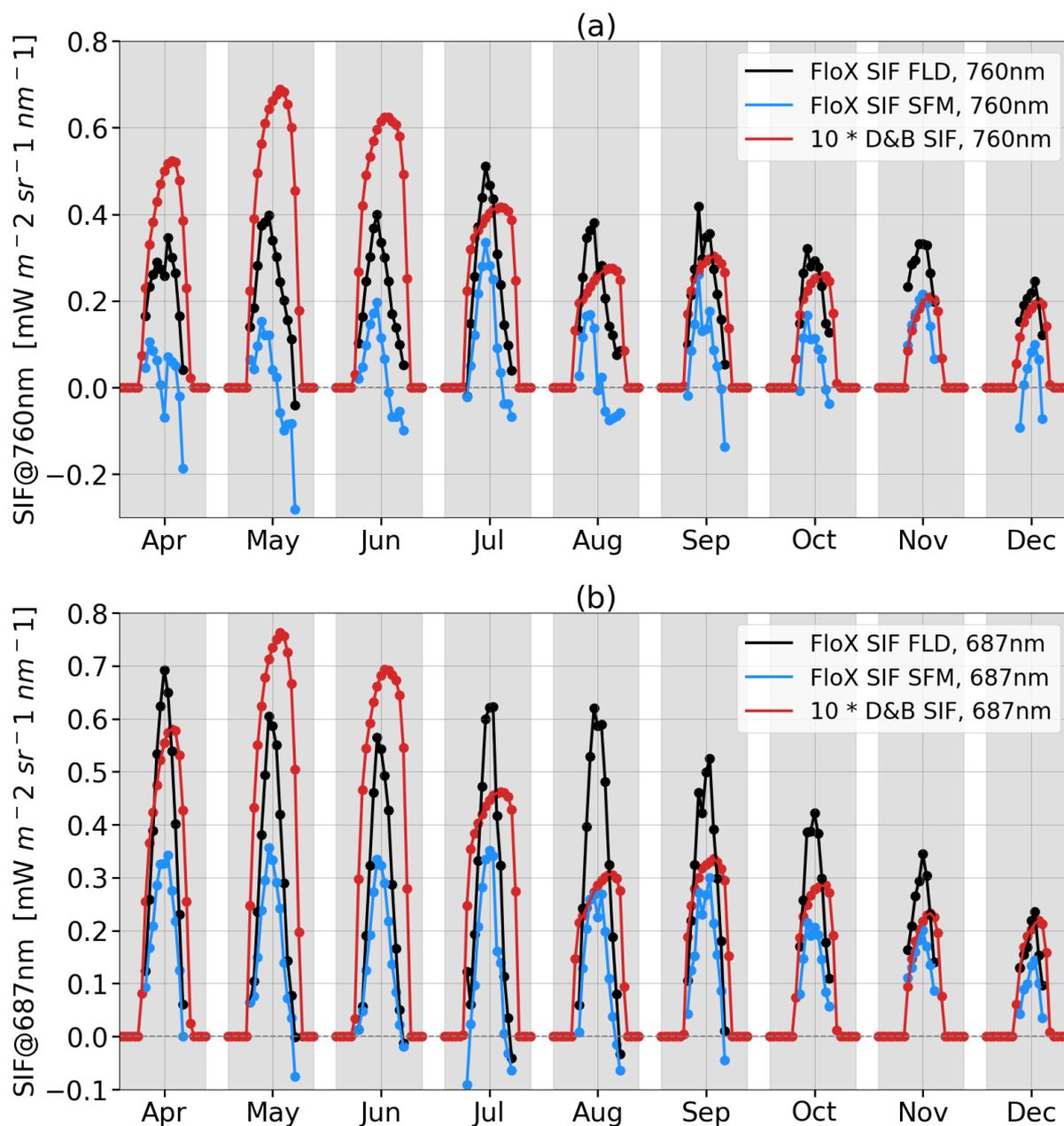
**Figure 10.** Average hourly diurnal cycle by month of SIF in the far-red (a) and red (b) for evergreen trees (PFT 3) at Majadas de Tietar for months April to December in 2021. D&B simulations (red) against measurements: retrievals made with Frauenhofer line discrimination (black) and spectral fitting method (blue).
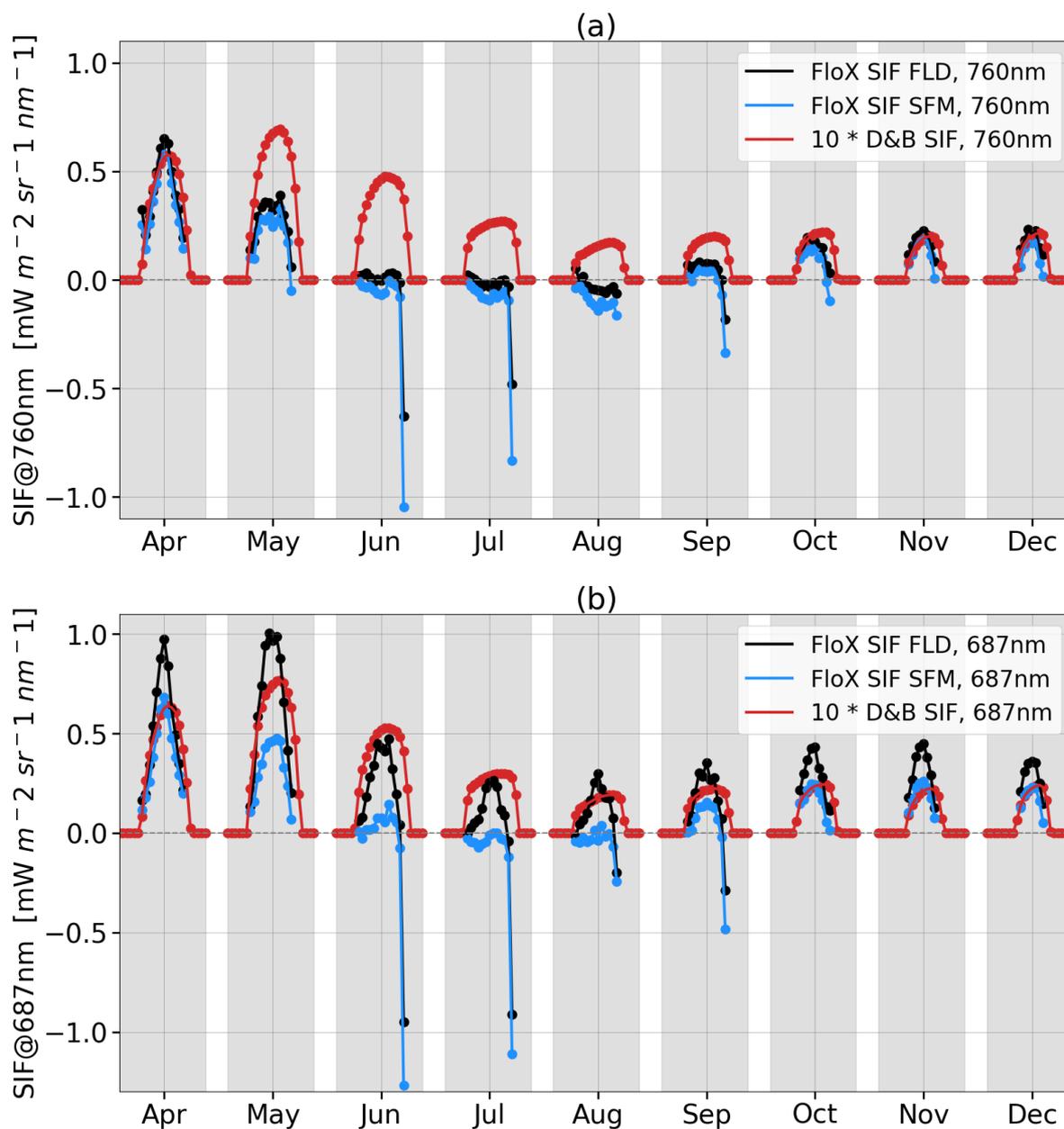
**Figure 11.** Average hourly diurnal cycle by month of SIF in the far-red (a) and red (b) for C3 grass (PFT 9) at Majadas de Tietar for months April to December in 2021. D&B simulations (red) against measurements: retrievals made with Frauenhofer line discrimination (black) and spectral fitting method (blue).
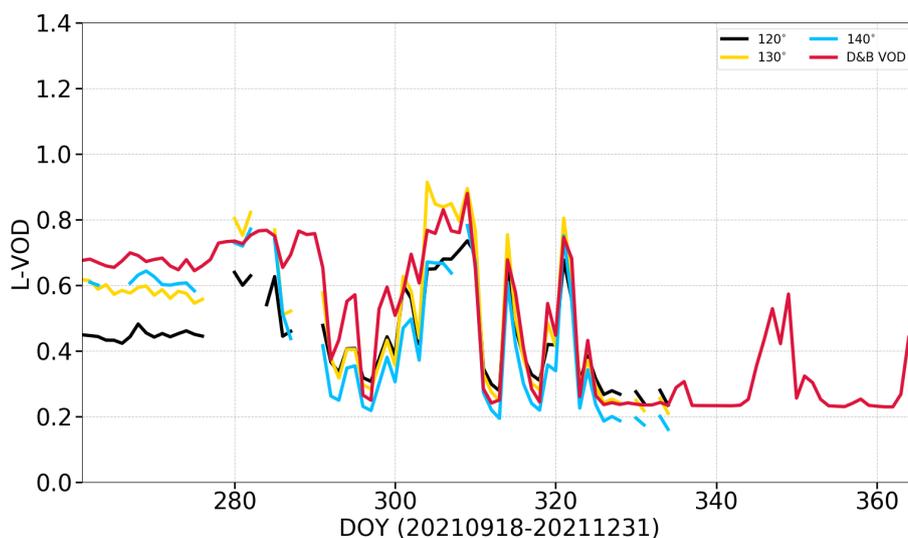
**Figure 12.** L-band VOD from Elbara II over a pine stand (PFT 5) for different elevation angles compared to D&B simulated L-band VOD, for PFT 5 only. Time axis starts on 18 September 2021 when the azimuth angle of the Elbara II instrument was changed for the first time.
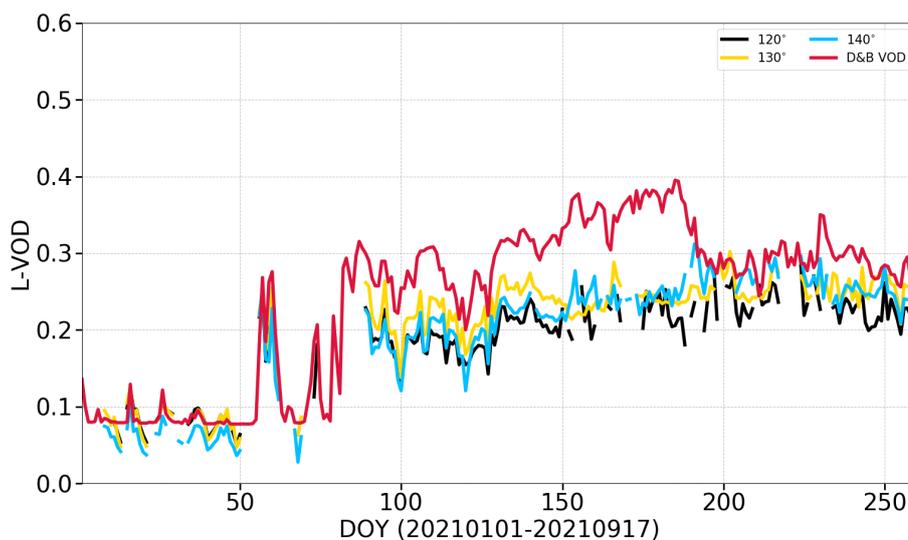
**Figure 13.** L-band VOD from Elbara II over a pine stand (PFT 5) for different elevation angles compared to D&B simulated L-band VOD, for PFT 5 only, before first change in view geometry, with biomass reduced to 1/3 of default simulated values.
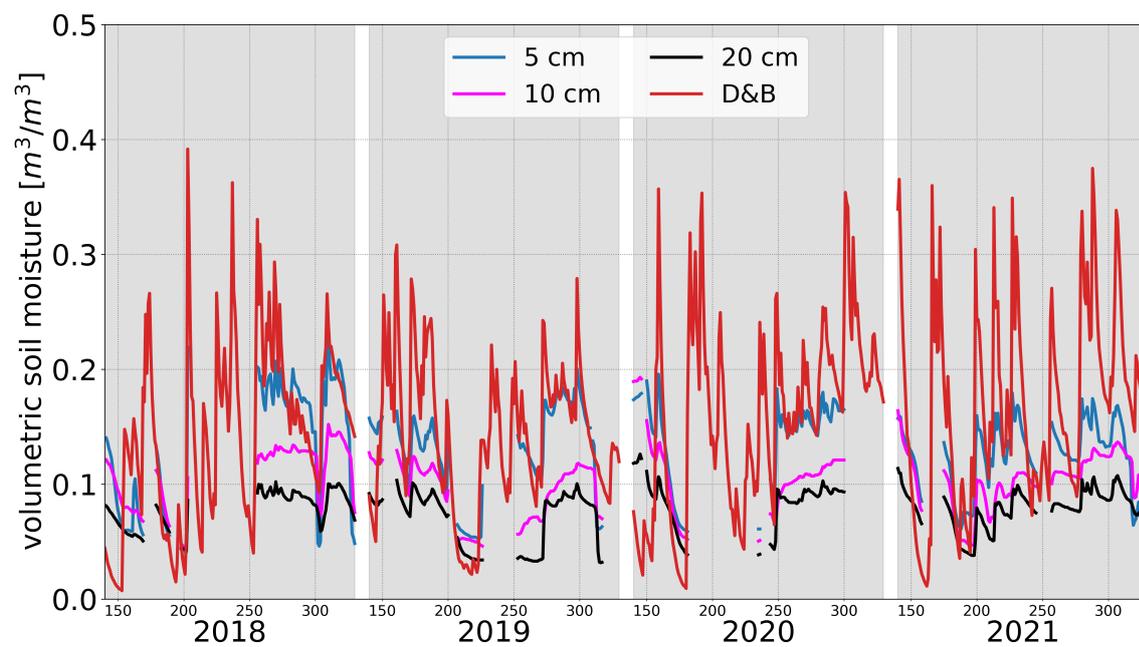
**Figure 14.** Daily *in situ* observed soil moisture at 5cm, 10cm and 20cm depth, and simulated near-surface soil moisture, $W_s$, at Sodankylä for Day-Of-Year 140—330 in the years 2018–2021. Winter months not shown to avoid impact of frost on soil moisture sensors.
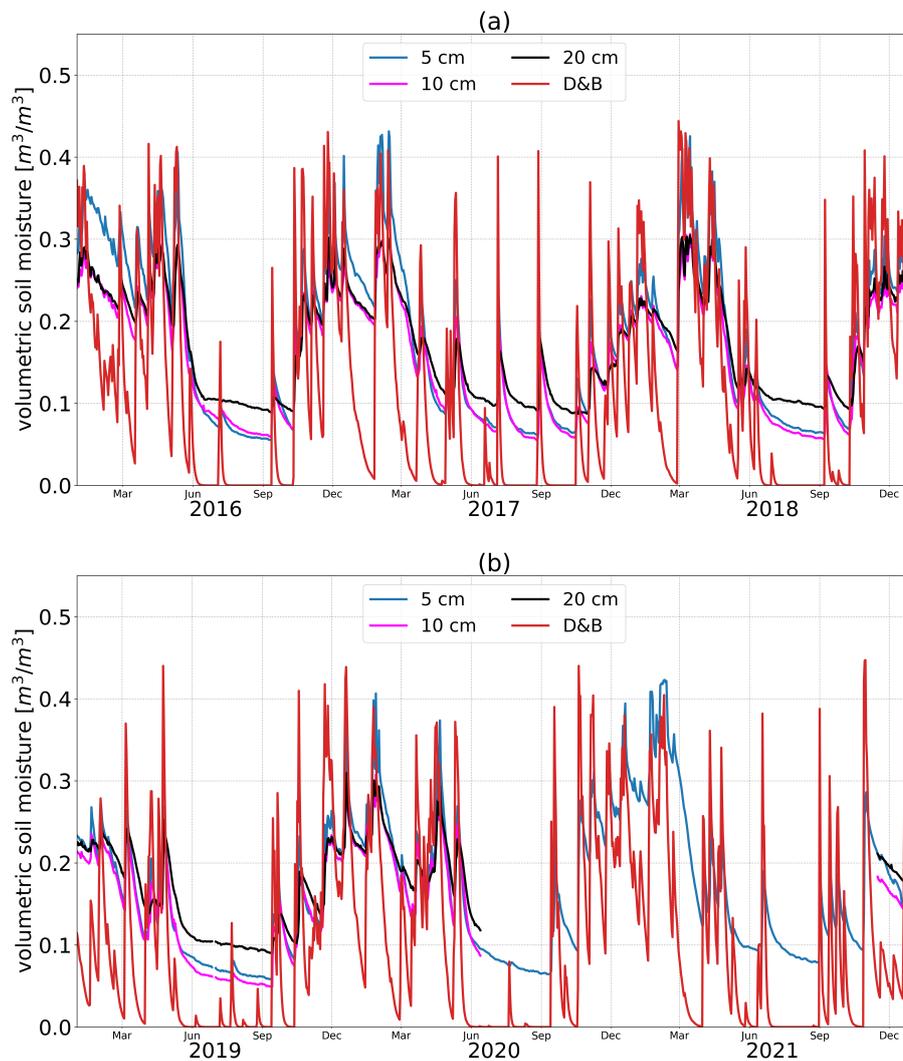
**Figure 15.** Daily *in situ* observed soil moisture at 5cm, 10cm and 20cm depth, and simulated near-surface soil moisture, $W_s$, at Majadas de Tietar for years 2016–2018 (a) and 2019–2021 (b).